The Astronomical Journal, 125:3145–3164, 2003 June

THE CANADIAN GALACTIC PLANE SURVEY

A. R. Taylor, S. J. Gibson, and M. Peracaula[1]
Department of Physics and Astronomy, University of Calgary, Calgary, AB T2N 1N4, Canada

P. G. Martin
Canadian Institute for Theoretical Astrophysics, University of Toronto, 60 St. George Street, Toronto, ON M5S 3H8, Canada

T. L. Landecker, C. M. Brunt, P. E. Dewdney, S. M. Dougherty, A. D. Gray, L. A. Higgs, C. R. Kerton, L. B. G. Knee, R. Kothes, C. R. Purton, B. Uyaniker,[2] B. J. Wallace,[3] and A. G. Willis
Dominion Radio Astrophysical Observatory, Herzberg Institute of Astrophysics, National Research Council of Canada, Box 248, Penticton, BC V2A 6J9, Canada

and

D. Durand
Canadian Astronomy Data Centre, Herzberg Institute of Astrophysics, National Research Council of Canada, 5071 West Saanich Road, Victoria, BC V9E 2E7, Canada
Received 2002 March 18; accepted 2003 March 12

ABSTRACT

The Canadian Galactic Plane Survey (CGPS) is a project to combine radio, millimeter, and infrared surveys of the Galactic plane to provide arcminute-scale images of all major components of the interstellar medium over a large portion of the Galactic disk. We describe in detail the observations for the low-frequency component of the CGPS, the radio surveys carried out at the Dominion Radio Astrophysical Observatory (DRAO), and summarize the properties of the merged database of surveys that comprises the CGPS. The DRAO Synthesis Telescope surveys have imaged a 73° section of the Galactic plane, using ~85% of the telescope time between 1995 April and 2000 June. The observations provide simultaneous radio continuum images at two frequencies, 408 and 1420 MHz, and spectral-line images of the $\lambda = 21$ cm transition of neutral atomic hydrogen. In the radio continuum at 1420 MHz, dual-polarization receivers provide images in all four Stokes parameters. The surveys cover the region $74.^{\circ}2 < l < 147.^{\circ}3$, with latitude extent $-3.^{\circ}6 < b < +5.^{\circ}6$ at 1420 MHz and $-6.^{\circ}7 < b < +8.^{\circ}7$ at 408 MHz. By integration of data from single-antenna observations, the survey images provide complete information on all scales of emission structures down to the resolution limit, which is just below $1' \times 1' \csc \delta$ at 1420 MHz and $3.'4 \times 3.'4 \csc \delta$ at 408 MHz. The continuum images have a dynamic range of several thousand, yielding essentially noise-limited images with an rms of ~0.3 mJy beam^{-1} at 1420 MHz and ~3 mJy beam^{-1} at 408 MHz. The spectral-line data are noise limited with rms brightness temperature $\Delta T_B \sim 3$ K in a 0.82 km s^{-1} channel. The complete CGPS data set, including the DRAO surveys and data at similar resolution in ^{12}CO (1–0) and in infrared emission from dust, all imaged to an identical Galactic coordinate grid and map projection, are being made publicly available through the Canadian Astronomy Data Centre.

Key words: Galaxy: general — ISM: general — ISM: structure — surveys

1. INTRODUCTION

Understanding the origin and evolution of galaxies is a central theme of modern astronomy. Galaxies evolve by the condensation and processing of the diffuse material in the interstellar medium (ISM) through multiple generations of stars. The ISM of a galaxy is both the source of the next generation of stars and the matrix within which the physical and chemical tracers of current and past generations appear. The conditions of the ISM, its spatial, dynamical, thermal, and chemical structure, reflect the evolutionary processes at work within a galaxy. Understanding the ISM is thus key to understanding galaxy evolution.

Our own Galaxy offers the only opportunity to observe these ISM processes in detail, but our location, completely embedded within the Galactic ISM, provides both opportunity and challenge. The ISM is a complex, dynamic medium, with structures in temperature, density, and velocity over a broad range of spatial scales. It consists of multiple phases: gas in atomic and ionized forms, dense pockets where the gas is molecular, and dust grains. The whole is threaded by magnetic fields and a flux of cosmic-ray particles. To sample the range of spatial scales from parsecs, typical of stellar separation and clustering, to kiloparsecs, characteristic of spiral arm systems, requires a high spatial dynamic range—an angular resolution of approximately 1′ coupled with sky coverage of several tens of degrees. The multiple phases of the ISM are rendered visible by observations over a range of wavelengths sensitive to different emission mechanisms. In 1995 a group of researchers in Canada and in other countries joined together to meet these requirements by creating a combined database of multiwavelength images over a significant fraction of the plane of the Galaxy with an angular resolution of about 1′. Data on all major components of the

[1] Current address: Departament d'Astronomia i Meteorologia, Universitat de Barcelona, Avenida Diagonal 647, E-08028 Barcelona, Spain.
[2] Current address: Max-Planck-Institut für Radioastronomie, D-53121 Bonn, Auf dem Hügel 69, Germany.
[3] Current address: Space Systems and Technology, Defence Research Establishment–Ottawa, 3701 Carling Avenue, Ottawa, ON K1A 0Z4, Canada.

ISM are provided by surveys at radio (atomic hydrogen, magnetic fields, and ionized and relativistic plasma), millimeter (molecular gas), and infrared (dust and policyclic aromatic hydrocarbons).

A particular observational challenge is the low-frequency, radio observations, where existing single-dish surveys, while providing high sensitivity and extensive sky coverage, yield very poor angular resolution relative to high-frequency observations. The most recent large-area survey of atomic hydrogen is that of Hartmann & Burton (1997), with an angular resolution of 36′. The low-frequency components of the Canadian Galactic Plane Survey (CGPS) are obtained with the Synthesis Telescope at the Dominion Radio Astrophysical Observatory (DRAO), which has 1′ resolution at 1420 MHz. Following a pilot study carried out in 1994/1995 (Normandeau, Taylor, & Dewdney 1997), the DRAO embarked on the CGPS project in 1995 April. By 2000 April a region of 660 deg^2 along the Galactic plane in the second quadrant had been observed, imaging in the radio continuum at 408 and 1420 MHz and in the 21 cm H I line. All the DRAO data products integrate single-antenna and interferometer data to provide high-fidelity images with complete sampling of structures on all angular scales larger than the resolution limit.

The DRAO atomic hydrogen survey is the first large-scale spectroscopic survey made with an aperture synthesis radio telescope. The region covered by the DRAO survey is largely limited to the outer Galaxy by the high declination limit of the east-west interferometer. Upon completion of observing for the first 660 deg^2 of the DRAO survey, an international collaboration was formed to create an H I survey covering almost the entire disk of the Galaxy by combining data from the Southern Galactic Plane Survey (Dickey et al. 1999) and the VLA Galactic Plane Survey (Taylor et al. 2002). All of these surveys have similar angular resolution and spectral resolution. As part of this collaboration, the DRAO surveys have been extended beyond the original 660 deg^2 in both longitude and latitude.

This paper describes in detail the acquisition and processing of the DRAO observations and the data products for the initial 660 deg^2 survey. Since the complete CGPS database for this initial survey has now entered the public domain, we present details relevant to the use of the CGPS data for astronomical research. Descriptions of the observations that have provided the other CGPS data sets at ^{12}CO (1–0) and far-infrared are published elsewhere (Heyer et al. 1998; Cao et al. 1997; Kerton & Martin 2000), and here we summarize the properties of the other data products and describe the additional processing carried out to produce the CGPS data. We present some examples of CGPS images and the details of the format of the CGPS data products, consisting of a series of images of all the survey data sets on a common grid and coordinate projection.

2. DRAO SYNTHESIS TELESCOPE OBSERVATIONS

2.1. *Single-Field Synthesis*

The DRAO Synthesis Telescope is described in detail by Landecker et al. (2000). Here we give a brief description of the telescope, concentrating on the parameters that define the properties of the survey. The telescope consists of seven equatorially mounted paraboloidal antennas on an east-west baseline with a maximum separation of 617.1 m. All

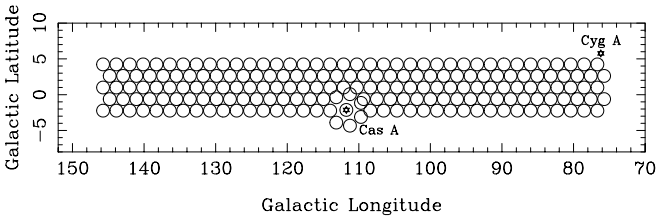

FIG. 1.—Grid of DRAO Synthesis Telescope observations. Each circle represents one synthesis field with diameter equal to the FWHM of the 1420 MHz primary beam (data from a larger area are used in making mosaics; see text and Fig. 5 for details). The survey area is covered by 193 synthesis pointings, each requiring 144 hr of observation over 12 array configurations. The hexagonal grid contains five rows of fields separated by 1.°62 in Galactic latitude with the central row at $b = -1°$. To allow high-sensitivity imaging around the position of the very strong radio source Cas A ($l = 111.°7$, $b = -2.°7$), the surrounding seven fields were repositioned to place Cas A close to the null of the 1420 MHz primary beam.

antennas have prime-focus feeds and simultaneously receive radiation at 1420 MHz in both right-hand (R) and left-hand (L) circular polarizations and at 408 MHz in R.

The small diameter of the array antennas (∼9 m) provides a wide synthesis field of view with an FWHM of 107.′2 at 1420 MHz and 332.′1 at 408 MHz. The survey area of 660 deg^2 was covered by observing a hexagonal grid of 193 synthesis fields, with a spacing between field centers of $\Delta = 112'$. The survey grid, shown in Figure 1, is laid out in Galactic coordinates with five rows of 38 fields. The central row lies at 1° Galactic latitude, to follow the midplane of the neutral hydrogen disk in the second quadrant of the Galaxy. The spacing between rows in Galactic latitude is $\sqrt{3}\Delta/2 = 1.°62$. The field-center separation is 1.04 times the FWHM of the primary beam at 1420 MHz and 0.34 times the 408 MHz beam. This value of the grid spacing was chosen as a compromise between uniform sensitivity (see § 3.5) and area coverage at 1420 MHz. In order to image the area around Cas A with the best dynamic range, the regular grid was abandoned and fields were placed so that Cas A was in the first null of the primary beam at 1420 MHz.

Three of the seven antennas are movable along a precision railway track. A full synthesis of an individual field is obtained by carrying out 12 individual 12 hr observations. Between each observation, the array configuration is changed by shifting the positions of the three movable antennas as a unit by an increment of $\Delta d = 4.29$ m. Over the duration of a full synthesis, all baselines from 12.9 to 604.3 m are sampled with a regular grid spacing of 4.29 m. The outer baseline of 617.1 m is also sampled. In order to maximize observing efficiency, a set of seven fields is observed at one array configuration 24 hr per day over 4 days, with half a day set aside for moving antennas and general maintenance. In principle, a full synthesis can be obtained of seven fields in 48 days. However, repeat observations and downtime mean that, in practice, it takes an average of about 56 days for a set of seven fields, allowing the observation of typically 46 fields per year. Observations began in 1995 April and were completed in 2000 June.

At 1420 MHz the R and L circular polarization signals are each split into five subbands, with two 7.5 MHz continuum bands located on either side of a central 5 MHz band that is fed into the spectrometer (discussed below). The continuum bands are centered at $\nu \pm 6.25$ and $\nu \pm 13.75$ MHz, where ν is the (tunable) center frequency of

the spectrometer, nominally the neutral hydrogen spin-flip frequency of 1420.406 MHz. The four continuum bands are correlated separately, forming all polarization products (RR, LL, RL, LR) on each baseline, allowing recovery of all four Stokes parameters (I, Q, U, V). The 256-channel spectrometer operates in both R and L and for the CGPS was set to receive a total bandwidth of 1 MHz, providing a velocity range of 211 km s^{-1}, with a channel separation of 0.824 km s^{-1} and a velocity resolution of 1.32 km s^{-1}. The 1420 MHz system temperature is 60 K. The 408 MHz system receives a single channel of right-hand circular polarization over a 3.5 MHz band with a system temperature of about 150 K (including the contribution from the typical sky brightness temperature).

At declination δ, the main lobe of the synthesized beam has dimensions $2\farcm8 \times 2\farcm8 \,\mathrm{cosec}\,\delta$ at 408 MHz and $49'' \times 49'' \,\mathrm{cosec}\,\delta$ at 1420 MHz. The theoretical rms noise at the pointing center in the continuum data is 3.0 mJy beam^{-1} (0.75 sin δ K) at 408 MHz and 0.28 mJy beam^{-1} (71 sin δ mK) at 1420 MHz. Measured noise values are 3.8 and 0.27 mJy beam^{-1}, respectively. The first grating lobe of the synthesized beam occurs at an angular radius in right ascension from the pointing center of $\theta_g = \lambda/\Delta d$, equal to $9\fdg8$ at 408 MHz and $2\fdg8$ at 1420 MHz. This is much larger than the angular distance to the 10% point of the primary beam of $\sim 4\fdg8$ at 408 MHz and $\sim 1\fdg5$ at 1420 MHz. The first grating ring associated with a source within one primary beam FWHM of the pointing center will lie outside the imaged area.

A clean synthesized beam is particularly important for synthesis of wide fields within the plane of the Galaxy where strong extended emission is common. This is especially true of H I data, where emission is present everywhere and covers all spatial scales. For the H I data the maximum sidelobe of the dirty beam is further reduced by applying a Gaussian taper to the u-v data with attenuation to 20% at the maximum baseline. A crosscut of the 1420 MHz spectral-line synthesized beam is shown in Figure 2. Beyond the region directly adjacent to the main lobe, the highest sidelobe in the synthesized beam falls below 0.5% everywhere in the field. Because of the taper, the synthesized beam for the H I line images is $58'' \times 58'' \,\mathrm{cosec}\,\delta$, slightly broader than the continuum beam. The theoretical rms noise in an empty channel at the pointing center is 20 mJy beam^{-1} (3.5 sin δ K). The measured value is 18 mJy beam^{-1}.

With 256 spectral channels, the channel width of 0.824 km s^{-1} was chosen to maximize the spectral resolution while still providing sufficient total velocity coverage to sample the full range of bright H I emission. The central velocity of the 211 km s^{-1} window was shifted as a function of longitude to encompass the velocity range of emission above 3 K as observed in the Leiden–Green Bank H I survey (Burton 1985). Above $l = 100°$, the central velocity in the local standard of rest (LSR) frame is $V_{\rm LSR} = -60$ km s^{-1}. Below $l = 100°$, the central velocity increases linearly to -46.8 km s^{-1} at $l = 75°$. Over the declination range of the observations (36°–67°), the rms noise level in brightness temperature for an empty channel ranges from 2.1 to 3.2 K.

The continuum bands at 1420 MHz span 35 MHz. Because of chromatic aberration, if the entire band were assumed to be at the nominal center frequency, there would be a reduction in the peak response of a point source by about 50% at an angular offset of $\rho = 90'$ from the pointing center, accompanied by a bandwidth smearing in the radial direction to approximately twice the nominal beamwidth. By processing the four 7.5 MHz continuum bands separately during imaging, the point-source peak flux density at $\rho = 90'$ is reduced by only 5%, with a comparable amount of radial source distortion (see Bridle & Schwab 1989). The 3.5 MHz band used at 408 MHz reduces the point-source sensitivity by about 10% at $\rho = 4\fdg8$. At these offsets the visibility-averaging period of 90 s produces a further reduction of the peak point-source response of about 8% in a 12 hr observation, with azimuthal smearing of the beam of similar magnitude. The combined effect with bandwidth smearing is then a worst-case reduction of point-source sensitivity of about 13% at 1420 MHz and 17% at 408 MHz, with both radial and azimuthal distortions. Since these values of ρ correspond to approximately the 10% point of the primary beams at both frequencies, data that are significantly affected enter into the final survey images with very low weight, and the resultant smearing is negligible.

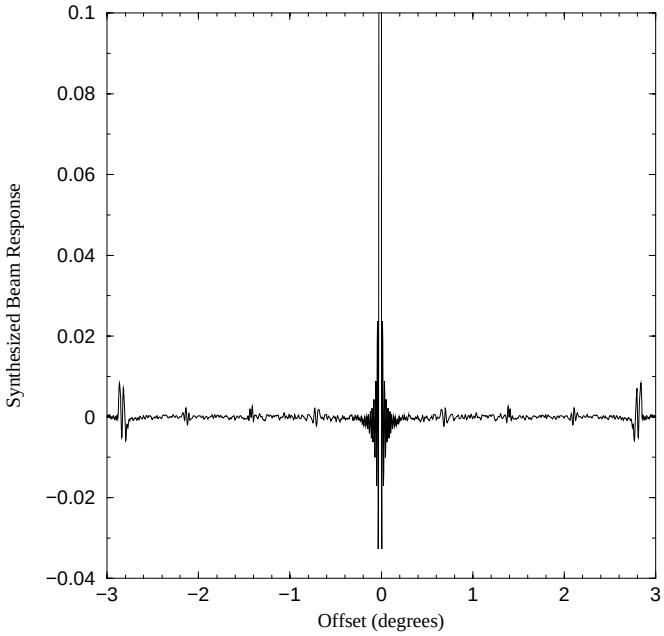

FIG. 2.—Cross section in right ascension of the 1420 MHz spectral-line synthesized beam. The first sidelobe of the dirty beam is ~3%. Away from the immediate vicinity of the main lobe, the response of the synthesized beam within the field of view is everywhere less than 0.5%.

2.2. *Calibration Observations*

2.2.1. *Complex Gain Calibration*

Complex gains for the pointing centers were calibrated by observing compact sources known to be temporally stable in both flux and structure on arcsecond scales. One such source was observed before and one after each 12 hr observing run at a given array configuration. Because of the wide field of view of the instrument, especially at 408 MHz, it is necessary to include a model of the sky surrounding the calibration source in the calibration process. A full synthesis observation was thus made of each calibration source. The calibrators used in the majority of observations are listed in Table 1. Fluxes are based on the Baars scale (Baars et al. 1977; Ott et al. 1994).

Calibration of total intensity is straightforward, with the mean antenna gain and phase parameters derived from the

TABLE 1
CALIBRATION SOURCES USED FOR THE SYNTHESIS OBSERVATIONS

Source	S_{408}	S_{1420}	p_{1420}	θ^p_{1420} (deg)
3C 48.....	38.9	15.7	0.6	...
3C 147.....	48.0	22.0	0	
3C 286.....	...	14.7	9.25	33.5
3C 295.....	54.0	22.1	0	

two calibrator observations being applied to the intervening target observation. Polarization calibration was achieved by using unpolarized sources (generally the same calibration observations) to correct the data for nonorthogonality of the R and L signals (i.e., leakage of R into the nominal L channel and vice versa), with observations of 3C 286 used to determine the absolute received polarization angle (Smegal et al. 1997).

2.2.2. *Bandpass Calibration*

Calibration of the spectrometer using astronomical signals is difficult because the narrow channel bandwidth leads to high noise levels in individual channels. Bandpass calibration was achieved in a two-step process. Gain and phase changes that affect the entire spectrometer band occur largely in antenna-based equipment, and experience shows that they can be satisfactorily calibrated from the observations used to calibrate the continuum channels of the telescope, made about every 12 hr. Channel-to-channel amplitude and phase differences arise largely in the filters that define the bandpass, just before the signals are digitized; these are quite stable with time. A common high-level noise signal was injected into the intermediate-frequency path from every antenna (both polarization channels), at a sufficient level to give an accurate measurement of gain and phase in each channel in 15 minutes. While this was done the antennas were pointed in different directions, so that signals from the sky do not correlate. The noise-injection bandpass calibration was performed once every 4 days.

2.2.3. *Wide-Field Polarimetry*

To correct the contamination from the total power, Stokes I, into Q and U across the field, an empirical model of the wide-field instrumental polarization was derived by observing polarized and unpolarized sources over a grid of locations within the primary beam. The strong, unpolarized sources 3C 295 and 3C 147 were observed at 88 positions over a rectangular grid with spacing of 15′, providing a measure of the instrumental polarization up to an offset of 75′ from the field center. Figure 3 shows contour plots of the instrumental component of each Stokes parameter as a percentage of I, averaged over the four 1420 MHz continuum subbands. The distribution of instrumental polarization across the field is the result of cross-polarization of the receiver feeds and the effects of the feed support struts. Because the Synthesis Telescope antennas have equatorial mounts, this instrumental polarization pattern is constant on the sky during a synthesis observation.

The wide-field polarization corrections were applied to polarization maps from each subband by interpolation of the corrections measured over the field. If $Q(l,m)_{\rm obs}$ is the flux at pixel (l,m) in the uncorrected Stokes Q map, $I(l,m)$ is the corresponding value in the Stokes I map, and $t(l,m)$ is the fractional instrumental polarization, then the corrected map is obtained via

$$Q(l,m)_{\rm corr} = Q(l,m)_{\rm obs} - t(l,m)\, I(l,m)\ . \qquad (1)$$

A similar correction is applied to the Stokes U maps.

We performed several tests to confirm the effectiveness of these corrections. To check for variation in the corrections, observations of 3C 295 over portions of the field were carried out on three separate occasions; in all cases the instrumental terms were identical to within the uncertainties. The polarized calibration source, 3C 286, was observed in five different offset directions; applying the wide-field correction successfully recovered the known values within errors. Finally, the consistency in polarization measurements was verified by comparison of data from the same source observed at different field positions in overlapping synthesis fields. Based on these measurements, the residual instrumental polarization error after correction is $\sim$0.3% at the field center and grows slowly to $\sim$1% at $\rho = 75'$.

3. IMAGE PROCESSING

3.1. *Removal of Residual Calibration Errors*

Calibrated continuum visibilities produce "raw" images that typically have a dynamic range of a few hundred. Further image processing uses routines developed especially for this telescope described by Willis (1999). The following describes the image-processing procedure that has been used to make continuum images with a dynamic range of up to 10,000 at 1420 MHz and up to 5,000 at 408 MHz. The need for special routines to achieve these performance levels arises from the telescope properties, particularly the wide fields of view.

Step 1. *Removing artifacts from strong sources outside the primary beam*.—Strong sources outside the primary beam can generate strong artifacts, particularly grating rings and, less frequently, radial spokes centered on the source. Since the offending sources come into the sidelobes of each individual antenna at a different level, and usually with a phase different from that applicable to the data in the center of the field, standard self-calibration cannot be used. The sources Cas A and Cyg A cause most of the problems in the CGPS survey area. These sources produce some level of contamination in virtually every 408 MHz image in the survey. The routine MODCAL (Willis 1999) derives a phase and amplitude for the response of each antenna to the offending source by fitting to the visibility data. The starting point for the fit is a set of theoretical visibilities based on a model of the source, generally derived from high-resolution images from other telescopes. These are modified to create time-dependent corrections to remove the effects of the source from the observed image.

Step 2. *Self-calibration*.—Phase and amplitude drifts over the 12 hr interval between calibrations are corrected with self-calibration. At 1420 MHz the dominant effect seems to be phase drifts on long timescales, although short-term phase and amplitude drifts can cause lower level defects, seen only in the vicinity of sources more intense than $\sim$3 Jy. At 408 MHz, long-term amplitude drifts are the dominant factor.

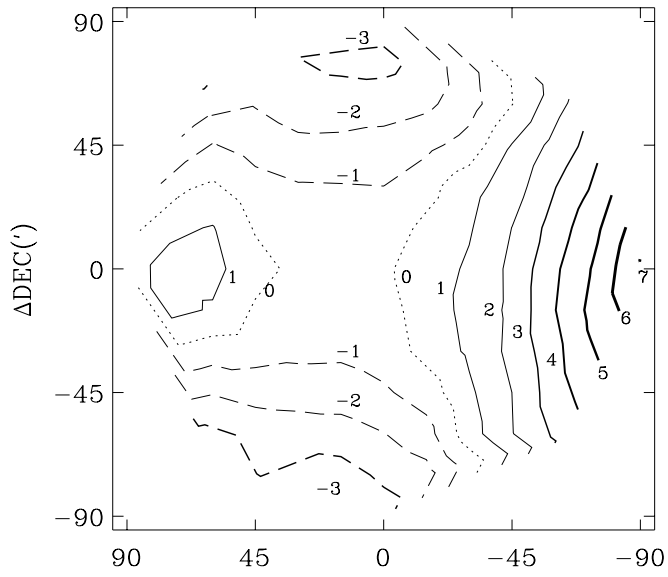

FIG. 3*a*

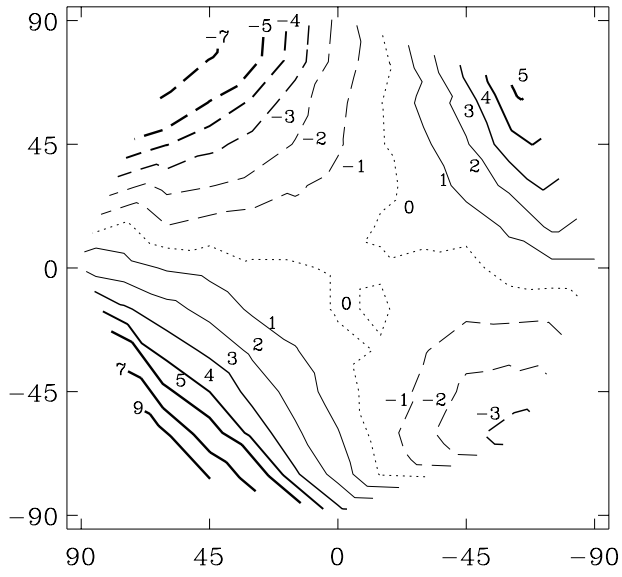

FIG. 3*b*

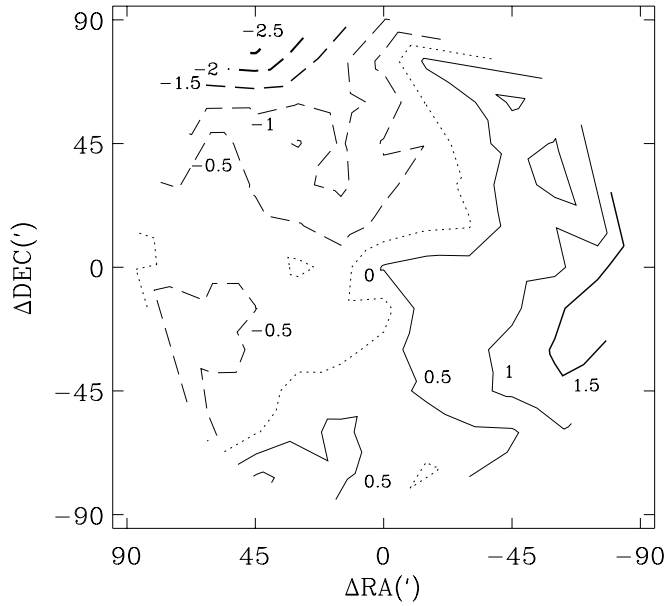

FIG. 3*c*

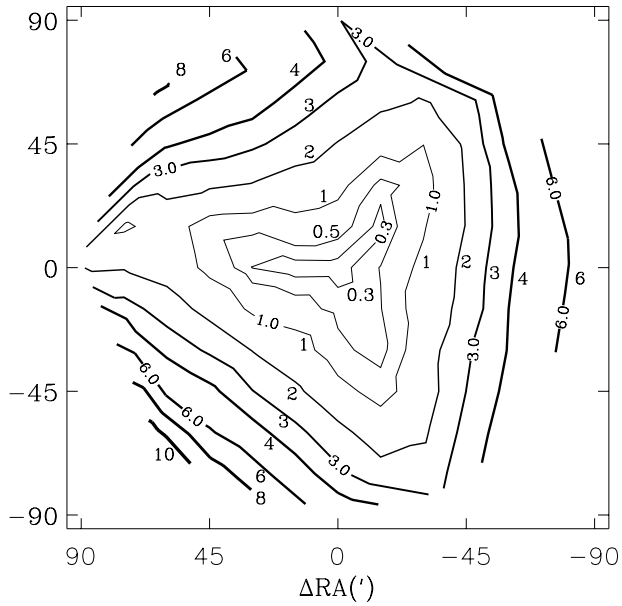

FIG. 3*d*

FIG. 3.—Contours representing percentage of (*a*–*c*) the Stokes parameters Q, U, and V, respectively, and (*d*) the linear polarized intensity $(Q^2 + U^2)^{1/2}$, all with respect to the total intensity I, from measurements of the unpolarized calibrators 3C 295 and 3C 147 at different positions within the synthesized field.

Complex gain corrections for the R and L receivers, derived for each antenna from self-calibration of the Stokes I data at 1420 MHz, were applied to the cross-correlation products, RL and LR, to construct the polarization images.

Step 3. *Removing remaining artifacts of sources within the primary beam.*—After self-calibration, many small-diameter sources still have surrounding ring artifacts; these are removed using MODCAL. The model used is based on CLEAN components from the source itself. This is applicable to sources whose flux density exceeds 30 mJy at 1420 MHz or 400 mJy at 408 MHz. For weaker sources the signal-to-noise ratio (S/N) is too low for successful fitting to visibilities. Since the typical source flux density in the polarization images is quite low, MODCAL is more rarely applied to polarization images.

Step 4. *Removal of weaker artifacts from sources outside the primary beam.*—Sometimes sources outside the primary beam create weak artifacts that must be removed by the MODCAL process at this stage. Examples are Cas A or Cyg A at very large radii. The Sun can also create artifacts. These primarily affect images at 408 MHz, because the sidelobe level at that frequency is relatively high; solar interference is rarely a problem at 1420 MHz. For removal from the images with MODCAL, the Sun is modeled to sufficient accuracy as a uniform disk.

Step 5. *Special CLEAN procedure around extended sources.*—Deep negative bowls occur around strong extended sources because of the lack of zero-spacing information. Residual rings around point sources in these bowls are "hidden" to processing methods because the peak of the source is lower than its true value and is sometimes still

at a negative level. To overcome this problem, we applied CLEAN separately to extended structure and fine structure. We first generated an image using only baselines with nominal lengths greater than 150 m (which contains only structure finer than about 4′). This image was CLEANed, and the CLEAN components were subtracted from the image computed using all visibilities. The resulting image contains only extended structure. This image was then CLEANed, and finally, the CLEAN components of the fine structure were added back.

It is not usually necessary to apply these techniques to spectral-line images, whose dynamic range is inherently low, limited by noise (typically 3 K on a single-channel image) and the peak brightness temperature (rarely above 120 K). The exceptions are those fields that contain strong continuum sources. Subtraction of a continuum image, derived from spectrometer channels free of H I signal (see §3.2), will in principle remove the continuum source and any artifacts around it. However, in certain channels continuum emission is absorbed; subtraction of the continuum image oversubtracts the artifacts in these channels. In such cases MODCAL was applied to remove residual artifacts from the line images (in practice this often proves necessary if the flux density of the continuum source exceeds about 1 Jy).

3.2. *Continuum Removal from* H I *Cubes*

Line-emission–free channels at one or both ends of the data cubes were averaged together to form an end-channel continuum map, which was then subtracted from the entire cube to form the line-emission–only data cubes. The choice of line-free channels was made by visual inspection of the data cube.

For the very occasional field where there are no obvious line-free channels, a matching continuum image was subtracted from the line data. The matching continuum image was created from data collected in the two continuum bands immediately adjacent to, and on either side of, the line emission band. These data were processed in the same manner as the line data and thus have identical *u-v* plane coverage. However, the total bandwidth of the matching continuum data (15 MHz) is much larger than the bandwidth of a single-line channel. As a result, the bandwidth smearing in the matching continuum map is larger than in a single-line channel. While the bandwidth smearing effects in the matching continuum map are small (the peak flux density of a point source at the 10% point of the beam is reduced by less than 5%), this can result in small residuals associated with subtraction of strong continuum sources.

3.3. *Field Registration*

The image processing, which involves phase and amplitude self-calibration, can produce slight position and flux-scale errors in individual fields. For this reason, an independent position and flux registration procedure was adopted to bring all the observations to a common absolute calibration. It should also be noted that the flux scale of the 408 MHz observations at DRAO is normally corrected based on the total radio power to remove the effect of an automatic gain control system. These corrections are not made for the CGPS observations. Instead, the registration procedure implicitly provides this correction. The procedure involves the comparison of properties of compact sources with their counterparts in catalogs from previous surveys of similar angular resolution.

All positions are tied to those of the NRAO VLA Sky Survey (NVSS; Condon et al. 1998), which in turn are based on the VLBI reference frame of Johnston et al. (1995). The 1420 MHz continuum and H I spectral-line fluxes are also registered to the NVSS catalog and depend ultimately on the absolute flux scale of Baars et al. (1977). Unfortunately, no prior calibrated survey was available for direct comparison at 408 MHz. Instead, these fluxes are scaled to values interpolated logarithmically between the 1420 MHz NVSS and 151 MHz Cambridge 7C(G) (Vessey & Green 1998) catalogs, with the latter tied to the flux scale of Roger, Bridle, & Costain (1973). Amplitude corrections reach a maximum of 20%–30% at both 1420 and 408 MHz. Maximum position corrections are a few arcseconds at 1420 MHz and a few tens of arcseconds at 408 MHz. The difficulties of absolute flux calibration at low frequency and possible spectral nonlinearity of the sources used for registration suggest an uncertainty of order 15% in the absolute 408 MHz flux scale. However, the internal consistency of the data is high, with median relative calibration errors of only ∼3%. This and other internal uncertainties are given in Table 2.

For each of the 193 fields, the 1420 MHz continuum, spectral line, and 408 MHz continuum data are registered separately. The end-channel continuum images are used for the H I line data. In each field, single-component sources with solitary catalog matches within 60″ and no additional matches within 120″ were identified as registration ensemble candidates. Those with half-power areas greater than 1.2 times the NVSS synthesized beam area were discarded to prevent any bias arising from different *u-v* coverages between DRAO and the reference catalogs. Sources with flux densities less than 5 mJy at 1420 MHz or 100 mJy at 408 MHz were also culled to minimize any mismatch of sensitivities between catalogs and observations. Finally, sources lying outside the main distribution of DRAO/reference flux ratios by more than 9 σ were deemed likely variables and ignored. All flux densities used throughout the registration procedure were integrated flux densities, which are immune to both bandwidth and azimuthal smearing effects. The 1420 and 408 MHz continuum fields typically included 50 sources after the above filtering, while the spectral-line end-channel continuum fields contained closer to 20.

Exceptions to these source counts occurred in the Cyg-X region at the low-longitude end of the survey, where acceptable compact sources are difficult to find. Here registration uncertainties are consequently larger, with the worst case obtained near $l = 80.^{\circ}3 \pm 1.^{\circ}0$, $b = -0.^{\circ}6 \pm 1.^{\circ}6$, where four adjacent fields yielded no usable sources in the 1420 MHz end-channel data because of the presence of strong extended continuum emission and contaminating line emission. These fields were flux-registered in the spectral line by a

TABLE 2
FIELD REGISTRATION UNCERTAINTIES

Data Set	σ_{RA} (arcsec)	σ_{decl} (arcsec)	σ_{flux} (%)
1420 MHz continuum	0.15	0.15	0.8
1420 MHz spectral line.....	0.40	0.40	3.0
408 MHz continuum	0.20	0.20	3.0

two-step method. First, the matching continuum image (see § 3.2) was flux-registered in the usual way to the NVSS scale (the absence of spectral-line emission in the matching continuum permitted a reasonable number of compact sources to be identified). Second, a ratio between the flux density scale of this image and that of the spectral-line end-channel continuum image was established from a pixel-by-pixel linear regression analysis; this fit was dominated by the extended continuum emission and served to tie the two intensity scales together.

An additional departure from the normal registration procedure was necessary for 408 MHz fields in the vicinities of the strong radio sources Cyg A and Cas A, where the coverage of 151 MHz reference catalog sources is sparse or absent altogether. CGPS fields in these areas were registered by comparing the positions and fluxes of sources they share with overlapping neighbor fields of known registration. The 408 MHz fields are large enough that useful overlap source sets exist between fields whose centers are separated by up to $\sim 5^\circ$. Some problem fields lie further than this from reference catalog sources; in this case, all fields within $\sim 5^\circ$ of reference sources were processed first, and their registrations were used to register subsequent sets of problem fields. Cumulative flux scaling errors of a few percent per overlap stage prevent this process from being extended indefinitely, but two overlap stages are sufficient to cover all 408 MHz problem fields in the CGPS.

Since the 408 MHz flux density registration scheme involves a two-point spectral interpolation, a further test was applied to remove sources with evidence of spectral curvature. The reference fluxes from the NVSS 1420 MHz and Cambridge 151 MHz catalogs, which were interpolated logarithmically to give the 408 MHz flux, were also interpolated to 365 MHz for comparison with the Texas survey of Douglas et al. (1996). Sources were removed if the interpolated flux deviated from the Texas flux by more than 4 σ or if the $S/N < 5$ in any of the three reference catalogs. As a cautionary note, however, the Texas catalog fluxes appear on average 15% brighter than those interpolated from the Cambridge and NVSS fluxes. This systematic difference was corrected before applying the curvature filter, but it indicates either a systematic spectral curvature in the sources used, a systematic discrepancy in low-frequency catalog flux scales, or both. For this reason, although the CGPS 408 MHz fluxes have high internal precision, their absolute scale is uncertain at the $\sim 15\%$ level.

After source ensemble filtering, the positional offsets and integrated flux ratios between observed and catalog values were averaged with appropriate weights to obtain several registration parameters. Corrections to the field-center position and mean flux scale were applied to each field. Average errors associated with these are given in Table 2. From a large ensemble of fields an average value was derived for field rotation, angular scaling, and primary beam attenuation as a function of offset ρ. All net field rotations were consistent with zero, indicating no measurable error in instrumental orientation about the pointing axis. For the spectral-line data, the radial stretch measure $\Delta\rho/\rho$ was likewise found to be zero within the uncertainties. Errors in the radial scale of the continuum images are $\Delta\rho/\rho$ of $(1.52 \pm 0.09) \times 10^{-4}$ and $(0.98 \pm 0.03) \times 10^{-4}$ for 1420 and 408 MHz, respectively. These arise from small deviations from the expected shape of the continuum bandpass, which bias the effective observed wavelength and subsequently the image scale. However, these stretches equate to maximum image distortions $\Delta\rho$ of $0\farcs8$ and $1\farcs7$ at the 10% point of the 1420 and 408 MHz primary beams, respectively, and thus have negligible effect on the final images. Finally, the change in flux scaling with radius from the field center was used to measure the primary beam attenuation pattern. This was found to be well fitted with a $\cos^6$ function, i.e.,

$$A(\rho) = \cos^6\left[\frac{2\rho\cos^{-1}(0.5^{1/6})}{\mathrm{FWHM}}\right], \qquad (2)$$

in agreement with past measurements but with the FWHM more accurately determined as $107\farcm2 \pm 0\farcm3$ at 1420 MHz and $332\farcm1 \pm 0\farcm8$ at 408 MHz.

3.4. *Integration of Low Spatial Frequency Information*

The low spatial frequency limit of a Synthesis Telescope observation is determined by the shortest antenna spacing used, $3\Delta d = 12.9$ m. This corresponds to an angular size scale of $\lambda/3\Delta d \approx 56'$ and $\sim 3\fdg3$ at 1420 and 408 MHz, respectively. Although foreshortening of the baselines during a synthesis observation provides some sampling of lower spatial frequencies, interferometric observations are generally not sensitive to structures on these angular scales and larger. To give complete spatial frequency coverage, the missing information on structures corresponding to low-order interferometer spacings must be obtained from observations using a filled aperture.

At 408 MHz, data from the all-sky map of Haslam et al. (1982) were used. Made from observations using a number of different large-aperture telescopes, this all-sky map has an effective resolution of $51'$. At 1420 MHz, surveys of the Galactic plane made with the Effelsberg 100 m telescope (Reich, Reich, & Fürst 1990, 1997) are the primary source of low-order spacing data (resolution $9\farcm4$). However, since these surveys do not adequately cover the upper Galactic latitude extent of our observations, interferometer fields along the high-latitude edge of the survey were supplemented with single-antenna data from the Stockert 25 m northern sky survey (Reich 1982; Reich & Reich 1986) with a resolution of $35'$. For the H I data, low-order spacing data were obtained from the single-antenna survey of the CGPS area (Higgs & Tapping 2000) with resolution of $36'$. These data were taken with the DRAO 26 m telescope and have been corrected for stray radiation.

The merging of single-antenna and interferometer data was done on a field-by-field basis before the mosaicking. For the H I data, low-order spacing information was added channel by channel. The single-antenna data were converted into visibilities by Fourier-transforming the single-antenna image and removing the single-antenna beam convolution by dividing by the transform of the beam profile. The image formed from the deconvolved single-antenna visibilities was multiplied by the Synthesis Telescope primary beam to produce a low-order spacing map that complements the high-order spacing map from the interferometer. The final step combines these two maps into a field with a complete set of spatial frequencies, by transforming the images and merging in the u-v plane using a normalized tapering function in the overlap region.

The low-order and high-order spacing maps have some spatial frequencies in common, and the extent of this

overlap in the *u-v* plane depends on the ratio between the shortest interferometer spacing s and the radius r of the single antenna. As a general guideline, it is desirable that $r \geq 2s$. This condition is satisfied only for the Effelsberg 100 m 1420 MHz continuum data. The remainder of the single-antenna data used in the CGPS is characterized by $r \simeq s$, providing continuous *u-v* plane coverage but a smaller range of overlap between the synthesis and single-antenna data.

Users of the CGPS DRAO data should be aware of two sets of artifacts arising from the single-antenna data. First, significant sidelobe effects appear near the bright radio sources Cas A and Cyg A. Their radius of influence is $\sim 1^\circ$–2° at 1420 MHz and up to $\sim 5^\circ$ at 408 MHz. The area around Cas A will be reobserved with the 100 m Green Bank Telescope; the unobstructed aperture of this telescope will reduce the sidelobe problem substantially. The second type of artifact is low-level striping that appears as discontinuities across lines of constant right ascension. The amplitude in the 408 MHz data is a few K, consistent with the quoted zero-level uncertainty of ± 3 K (Haslam et al. 1982). The effect is far less serious at 1420 MHz. The Effelsberg survey (Reich et al. 1990,1997) is free of scan artifacts, so stripes are not present for $b < 5^\circ$. The effect is seen only at latitudes $b > 5^\circ$, where it arises from zero-level effects in the Stockert data; Reich (1982) quotes an uncertainty of ~ 0.1 K. The artifacts can appear deceptively real when single-antenna and DRAO synthesis data are merged. Options for destriping these surveys are under investigation. Meanwhile, users of the CGPS DRAO images should be cautious about the interpretation of faint, large-scale ($\gtrsim 1^\circ$) features. The Higgs & Tapping (2000) survey has some stripe artifacts across lines of constant Galactic longitude at levels of ~ 1 K, but these are of sufficiently small angular size that they are removed in the filtering step of integrating with the synthesis data, and the final CGPS H I maps show no obvious stripe contamination.

3.5. *The CGPS Mosaics*

The processed DRAO fields were combined into 1024×1024 pixel mosaic images in FITS format on a Galactic Cartesian grid, which define the standard data format for all the CGPS data products. Since the data acquired in the DRAO survey fall into two resolution classes, near $1'$ (1420 MHz) and near $4'$ (408 MHz), two different sets of partially overlapping mosaic images were produced.

3.5.1. *The* $5^\circ \times 5^\circ$ *Mosaics*

At 1420 MHz the full area of the CGPS is covered by 36 mosaics, each $5\overset{\circ}{.}12 \times 5\overset{\circ}{.}12$ in extent, with enough overlap to allow objects or regions of interest less than 1° in size to be fully contained in one such mosaic. Each 1024×1024 mosaic has a pixel size of $18''$ in Galactic coordinates. This pixel size gives ~ 3.3 pixels per synthesized beam for 1420 MHz data. The mosaics overlap by $1\overset{\circ}{.}12$ and cover the 660 deg^2 defined by $l = 74\overset{\circ}{.}2$ to $147\overset{\circ}{.}3$, $b = -3\overset{\circ}{.}6$ to $5\overset{\circ}{.}6$. Figure 4 shows the layout of these mosaics (known as the **M**-mosaics), and Table 3 gives the Galactic coordinates of pixel (513, 513) of each of the mosaics. The terminology used for the mosaic codes is based on that used at DRAO to specify Synthesis Telescope fields.

For the H I data cubes, the number of channels, reference channel, reference-channel LSR velocity, and channel separation are given in Table 4. The number of channels, 272, results from the variation in LSR reference velocity with Galactic longitude used for the synthesis observations in order to keep the Galactic H I emission centered in the observational bandwidth. The correlators produce spectra in channels at uniform frequency intervals, not velocity, so there is a slight error in taking the channels to be velocity channels. The error so introduced is negligible, less than 0.04 of a channel at the extreme ends of the spectra.

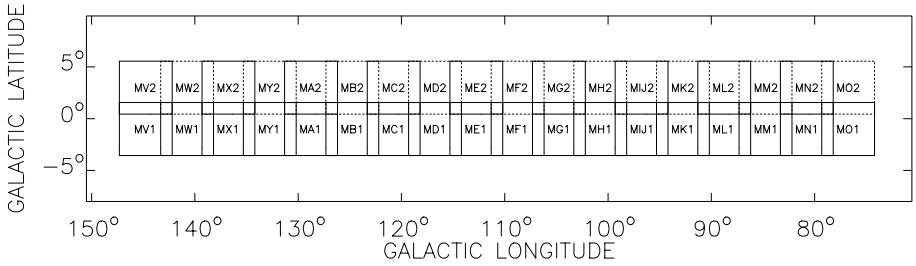

FIG. 4*a*

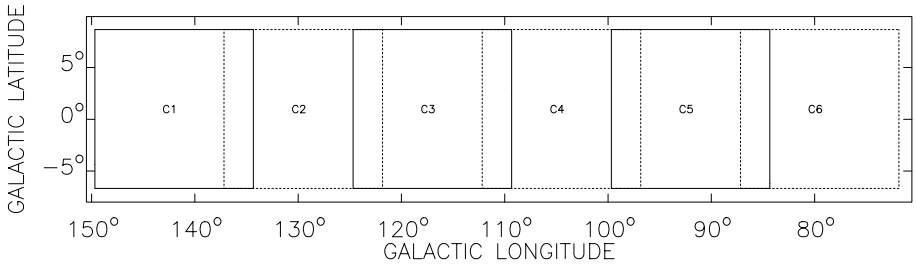

FIG. 4*b*

FIG. 4.—CGPS mosaic image layout. (*a*) The high-resolution data sets ($1'$ scale) are covered by the 36 $5\overset{\circ}{.}1 \times 5\overset{\circ}{.}1$ **M**-series mosaics. (*b*) At 408 MHz a series of six $15^\circ \times 15^\circ$ **C**-mosaics are also constructed. All mosaics are 1024×1024 samples in the (l, b)-plane. Spectral-line mosaics have 272 velocity planes separated by 0.82 km s^{-1}.

TABLE 3
THE 5° × 5° MOSAICS

Mosaic Code	Galactic Longitude (deg)	Galactic Latitude (deg)	Mosaic Code	Galactic Longitude (deg)	Galactic Latitude (deg)
MV1	144.75	−1	MV2	144.75	+3
MW1	140.75	−1	MW2	140.75	+3
MX1	136.75	−1	MX2	136.75	+3
MY1	132.75	−1	MY2	132.75	+3
MA1	128.75	−1	MA2	128.75	+3
MB1	124.75	−1	MB2	124.75	+3
MC1	120.75	−1	MC2	120.75	+3
MD1	116.75	−1	MD2	116.75	+3
ME1	112.75	−1	ME2	112.75	+3
MF1	108.75	−1	MF2	108.75	+3
MG1	104.75	−1	MG2	104.75	+3
MH1	100.75	−1	MH2	100.75	+3
MIJ1	96.75	−1	MIJ2	96.75	+3
MK1	92.75	−1	MK2	92.75	+3
ML1	88.75	−1	ML2	88.75	+3
MM1	84.75	−1	MM2	84.75	+3
MN1	80.75	−1	MN2	80.75	+3
MO1	76.75	−1	MO2	76.75	+3

3.5.2. *The* 15° × 15° *Mosaics*

As for all CGPS data products, **M**-series mosaics were also constructed from the 408 MHz data. However, the larger primary beam of the Synthesis Telescope at 408 MHz provides much greater sky coverage. In order to present the full area imaged at 408 MHz, a second set of larger mosaics was constructed at this frequency. They are also 1024 × 1024 pixels in extent, with a pixel size of 54″, giving ~3.9 pixels per synthesized beam and a dimension of 15°.36 on a side. The layout of these mosaics, known as the **C**-mosaics, is shown in Figure 4, and the Galactic coordinates of pixel (513, 513) of each mosaic are given in Table 5. These mosaics overlap in longitude by 2°.86.

3.5.3. *Creating the Mosaic Images*

The data from many Synthesis Telescope fields must be combined in order to create each of the mosaic images specified above. Data are included from each field out to a radius corresponding to the 10% point of the primary beam attenuation. At 1420 MHz, about eight Synthesis Telescope fields are major contributors (i.e., their pointing centers lie within the mosaic) to any of the **M**-mosaics, with approximately another nine Synthesis Telescope fields being minor contributors (their 10% attenuation points lie within the mosaic). The data from the overlapping fields were averaged together with suitable weights. An example of such overlapping fields is shown in Figure 5, where the fields used to produce the 1420 MHz mosaic MW1 are presented. Sixteen Synthesis Telescope observations contribute to this mosaic.

TABLE 4
THE SPECTRAL-LINE COORDINATE SPECIFICATIONS

Parameter	Value
Number of channels	272
Channel separation	−0.82446 km s^{-1}
Reference channel	145
Reference LSR velocity	−60 km s^{-1}

The DRAO mosaic images are presented in units of brightness temperature. The noise level in the mosaicked image is minimized when the sky brightness T_B in the mosaic is derived from

$$T_B = \sum_{m=1}^{N} w_m T_m \ , \tag{3}$$

where T_m is the primary-beam–corrected brightness temperature in field m. The weights w_m are

$$w_m = \left[\frac{A(\rho_m)}{\sigma_m} \right]^2 , \tag{4}$$

where $A(\rho_m)$ is the primary beam attenuation (eq. [2]) at the offset ρ_m of the pixel in field m, corresponding to the given sky position, and σ_m is the rms noise level at the center of map m. In general, σ_m is the same for all fields, with the exception of fields close to the strong sources Cas A and Cyg A. The rms noise level in the resulting mosaic is a function of position and is given by

$$\sigma = \left[\sum_{m=1}^{N} w_m^2 \right]^{-1/2} . \tag{5}$$

TABLE 5
THE 15° × 15° MOSAICS

Mosaic Code	Galactic Longitude (deg)	Galactic Latitude (deg)
C1	142.3	+1
C2	129.7	+1
C3	117.1	+1
C4	104.5	+1
C5	91.9	+1
C6	79.3	+1

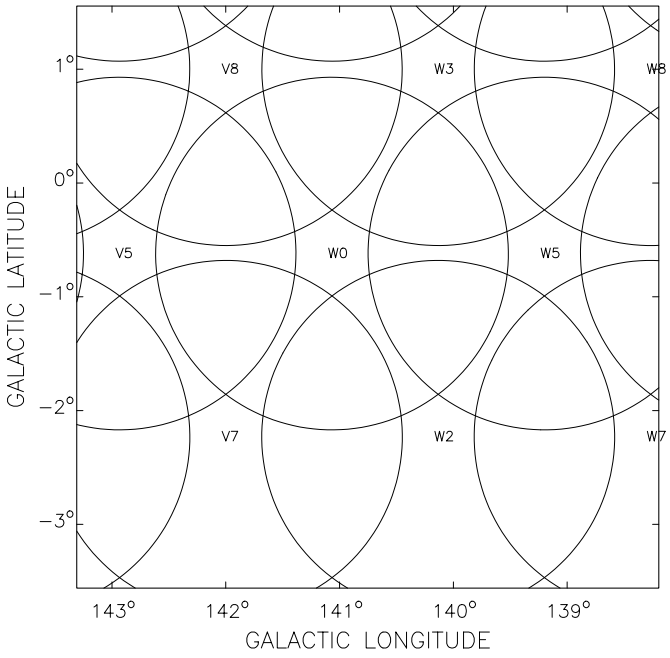

FIG. 5.—Synthesis Telescope fields used in creating the 1420 MHz MW1 mosaic. The field radii are defined by the 10% level of the primary beam ($\rho = 93'$). Sixteen synthesis fields contribute to this mosaic image.

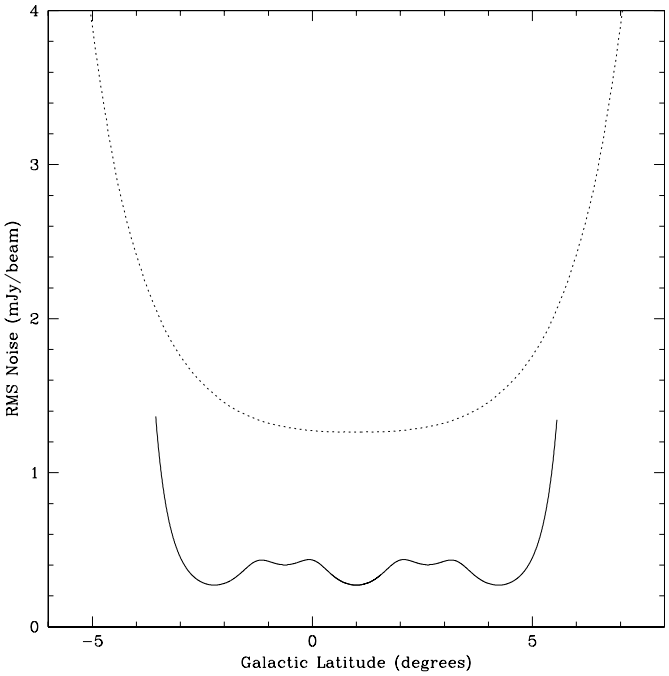

FIG. 6.—Theoretical noise level in the continuum mosaics for a sample cut in latitude across the survey grid. The solid curve shows the level at 1420 MHz. The theoretical noise has an average rms value of 0.34 mJy beam^{-1} within $-3° < b < +5°$. The theoretical noise limit is reached at 1420 MHz over most of the survey, with the exception of small regions around a few very strong sources (e.g., Cas A). The dotted curve shows the level at 408 MHz. At this frequency the theoretical minimum rms noise is 1.4 mJy beam^{-1}. However, in practice the image rms is limited to about 3 mJy beam^{-1} by confusion.

Figure 6 shows the theoretical rms noise level that can be achieved for a sample cut in Galactic latitude across the survey grid. At 1420 MHz a relatively uniform noise level with a minimum value of 0.27 mJy beam^{-1} and a mean level of 0.34 mJy beam^{-1} is obtained within an approximately 8° latitude strip from $-3° < b < 5°$. At 408 MHz a minimum noise level of 1.4 mJy beam^{-1} is theoretically possible within an area nearly the size of the 1420 MHz survey region. Outside of this area the theoretical rms noise is below 3 mJy beam^{-1} within a 13° strip $-4.°5 < b < +6.°5$. However, in practice the rms noise at 408 MHz is limited to ~3 mJy over the whole area by confusion and image dynamic range.

A mosaicking routine called SUPERTILE was written that combines a large number of input images or data cubes in various astronomical coordinate systems and velocity frames, producing a mosaic image or data cube in a given astronomical coordinate system and velocity frame. For the DRAO data, the input images are in the NCP coordinate system, the natural system for an east-west interferometer, while the output image is in Galactic coordinates. At each pixel/voxel of the output image/cube, a corresponding data value is interpolated from each of the input data sets, using a bicubic interpolation scheme in the spatial dimensions and linear interpolation in the velocity dimension, and assigned the corresponding weight w_m.

Corrections for several subtle effects are included in the data extraction. The images or data cubes corresponding to the individual fields observed with the Synthesis Telescope are in NCP pseudoequatorial coordinates. In these images, the synthesized beam is constant over the image, and the calibrated pixel intensities are in units of Jy beam^{-1}. During the addition of short-spacing data, these pixel intensities were converted to "pseudo–brightness temperature" simply by scaling by a factor constant over the image. However, when projected onto the real sky, the synthesized beam is not constant in solid angle. To first order, it varies as $\sin \delta_0 / \sin \delta$, where the declination of the field center is δ_0. To obtain true brightness temperatures on the sky, the pseudo–brightness temperatures in each field must be correspondingly corrected with a declination-dependent factor. This factor can vary as much as ±12% over the large 408 MHz field of view.

The velocity interpolation when merging data cubes must allow for the fact that spectral observations made with the Synthesis Telescope are correctly adjusted to the LSR only at the field center. Because of the wide field of view, the LSR velocity assigned to a given spectral channel, while correct at the field center, may be in error by as much as 1.2 channels at the field edge. During the interpolation process, the velocity of each voxel of the cube was adjusted to the correct LSR frame.

In addition to creating a mosaic image or data cube from the Synthesis Telescope data, SUPERTILE also produces a weight image that gives the total weight of each pixel of the mosaicked image, equal to the quadratic sum of the weights of the input images contributing to the pixel. This weight image can be used to create an image of the noise distribution across the mosaic (see eq. [5]). As shown in Figure 6, the theoretical noise level varies smoothly over the mosaic. In the 1420 MHz images the ratio of maximum to minimum noise level is 1.62. In the 408 MHz **M**-mosaics the ratio is 1.64.

The effective resolution also varies across a mosaic, because the effective synthesized beam is an average of the beams corresponding to each of the input images. For each mosaic, the SUPERTILE program produces two products

that give information on this variation. To give an overview of the beam variations, an image of beams was produced. This presents 289 beam patches (17×17) in a 272×272 pixel image, corresponding in area to the 1024×1024 mosaic, where each patch of 16×16 pixels displays the synthesized beam at that position in the mosaic. Quantitative information on the beam parameters is stored in a $17 \times 17 \times 5$ data cube that gives, for each of the 17×17 sample beams shown in the beam-patch image, the weight at that point in the corresponding mosaic, the beam solid angle (pixels^2), the beam major and minor half-power width (pixels), and the orientation angle of the major axis of the beam ellipse (degrees counterclockwise from Galactic west). This data cube is termed the "resolution-parameter cube."

4. PANORAMIC IMAGES OF THE DRAO SURVEY

To illustrate the properties of the DRAO data we have combined the 1420 MHz continuum and line mosaics to create panoramic images giving an overview of the entire survey region. These images are shown in Figures 7*a*–7*d*. The top panels display the 1420 MHz continuum emission and the bottom panels one channel of the H I data cube, at $V_{\rm LSR} = -40.21$ km s^{-1}.

4.1. *The 1420 MHz Continuum Image*

This image is a significant advance in radio astronomy surveys. In resolution and spatial frequency coverage it is the equivalent of the image that would be made with a 600 m single antenna. The spatial dynamic range, the ratio of the largest observable feature to the area of the resolution element, is approximately 2.5×10^6.

The signal dynamic range is also high. With the exclusion of the region around Cas A (blanked-out region at $l = 111\overset{\circ}{.}5$) and Cyg A ($l = 75^\circ$), the lowest detectable brightness is essentially limited by thermal noise of about 0.3 mJy beam^{-1}, despite the ubiquitous presence of strong emission with brightness of several Jy beam^{-1}. It is impossible to present the full range of the image as a gray scale on paper despite the use of a logarithmic scale. Gray scales were chosen to preserve details in some of the bright regions, and some large extended diffuse emission is barely visible even though it is well above the noise in the image.

Several large bright emission complexes "frame" the survey region, the Cyg-X complex, G80+1, blending into W80 (G85−1), and the W3/W4/W5/HB 3 complex, G135+1. These are dominated by thermal emission from H II regions, but there is a sprinkling of nonthermal emission from supernova remnants (SNRs).

There are some very large objects that are quite nearby, including the SNRs W63 (G82.2+5.3; partly off the top of the image) and HB 21 (G89.0+4.7) and the H II regions S131 (G99.3+3.7) and S171 (G118.4+4.7). There are several other large complexes of H II regions and SNRs, particularly one at $l \approx 94^\circ$ and one around Cas A.

Sixteen SNRs can be seen by inspection of the data as reproduced in the figures. Small, bright SNRs include the historic remnants Tycho (G120.1+1.4) and 3C 58 (G130.7+3.1). Of the more extended SNRs, the brightest are G78.2+2.1 (in Cyg-X), G84.2−0.8 (seen through W80), HB 21 (G89.0+4.7), and CTB 109 (G109.1−1.0). Among the fainter remnants, still imaged with excellent S/N, are CTB 1 (G116.6+1.1) and G114.3−0.3. Still fainter SNRs, not discernible in these figures, have been discovered in the images by Kothes et al. (2001).

A band of very diffuse emission runs the entire length of the survey. This is probably dominated by synchrotron emission from the thick disk of the Galaxy, mixed, at these lower latitudes, with thermal emission from diffuse ionized hydrogen. In Figures 7*a*–7*d* it is most easily seen from $l = 86^\circ$ to $l = 98^\circ$, peaking at about $b = 2^\circ$, and again around the entire complex of objects between $l = 102^\circ$ and $l = 114^\circ$.

4.2. *The* H I *Line Image*

The H I images in Figures 7*a*–7*d* are on a gray scale that is linear with intensity. The continuum emission has been subtracted from the image, leaving only atomic hydrogen emission, with the exception of continuum absorption signals such as seen quite strongly on W3 (G134+1). The darkest regions in these images correspond to brightness temperatures of ~125 K.

In the outer quadrants of the Galaxy the velocity-distance relationship from pure circular motion is monotonic. At the high-longitude end of the CGPS, $V_{\rm LSR}$ of −40.21 km s^{-1} corresponds to emission from gas in the Perseus arm, at a distance of ~2 kpc. The spatial resolution at this distance is 0.7 pc, and the 20° longitude interval of Figure 7*a* corresponds to a distance of 0.84 kpc.

Even in these single-velocity channels, H I emission has a large filling factor and exhibits structures on all scales down to the resolution limit. "Filaments" of H I emission that are unresolved perpendicular to their lengths are common. Such filaments are often seen as elements of coherent structures that persist for several degrees and more, or hundreds of parsecs. The H I medium seen at parsec-scale resolution has the general appearance of a dynamic, energized medium.

The H I images contain several features that have been discovered and analyzed using the CGPS data and reported elsewhere. Figure 7*a* contains one velocity channel of the Galactic chimney rising above the H II region W4 at $l = 135^\circ$ (Normandeau, Taylor, & Dewdney 1996). The winds of the cluster of massive stars ionizing W4 have blown a vertical channel in the ISM, allowing ionizing radiation to escape to the Galactic halo (Dennison, Topasna, & Simonetti 1997). In the nearby intense H I emission at $l = 139^\circ$ bright lanes (of less intense emission) appear, arising from cold hydrogen clouds absorbing the background emission (Gibson et al. 2000). These cold, dense clouds may represent the result of compression of diffuse hydrogen in the wake of the Perseus arm spiral shock (Gibson 2002). In Figure 7*b* the stem and part of the cap of a mushroom-shaped atomic hydrogen cloud is seen extending toward negative latitudes at $l = 124^\circ$ (English et al. 2000). This cloud, of unknown origin, is an example of bulk mass transfer between the midplane and the thick disk or halo of the Galaxy. It appears on the edge of a region $110^\circ < l < 124^\circ$ characterized by the presence of large-scale H I structures extending out of the midplane. These structures may be related to energy injection due to massive star formation evidenced by the clusters of supernova remnants seen in the continuum image over these longitudes.

This series of images illustrates that large-scale maps of atomic hydrogen emission at arcminute resolution reveal the H I gas as a tracer of dynamical processes in the ISM.

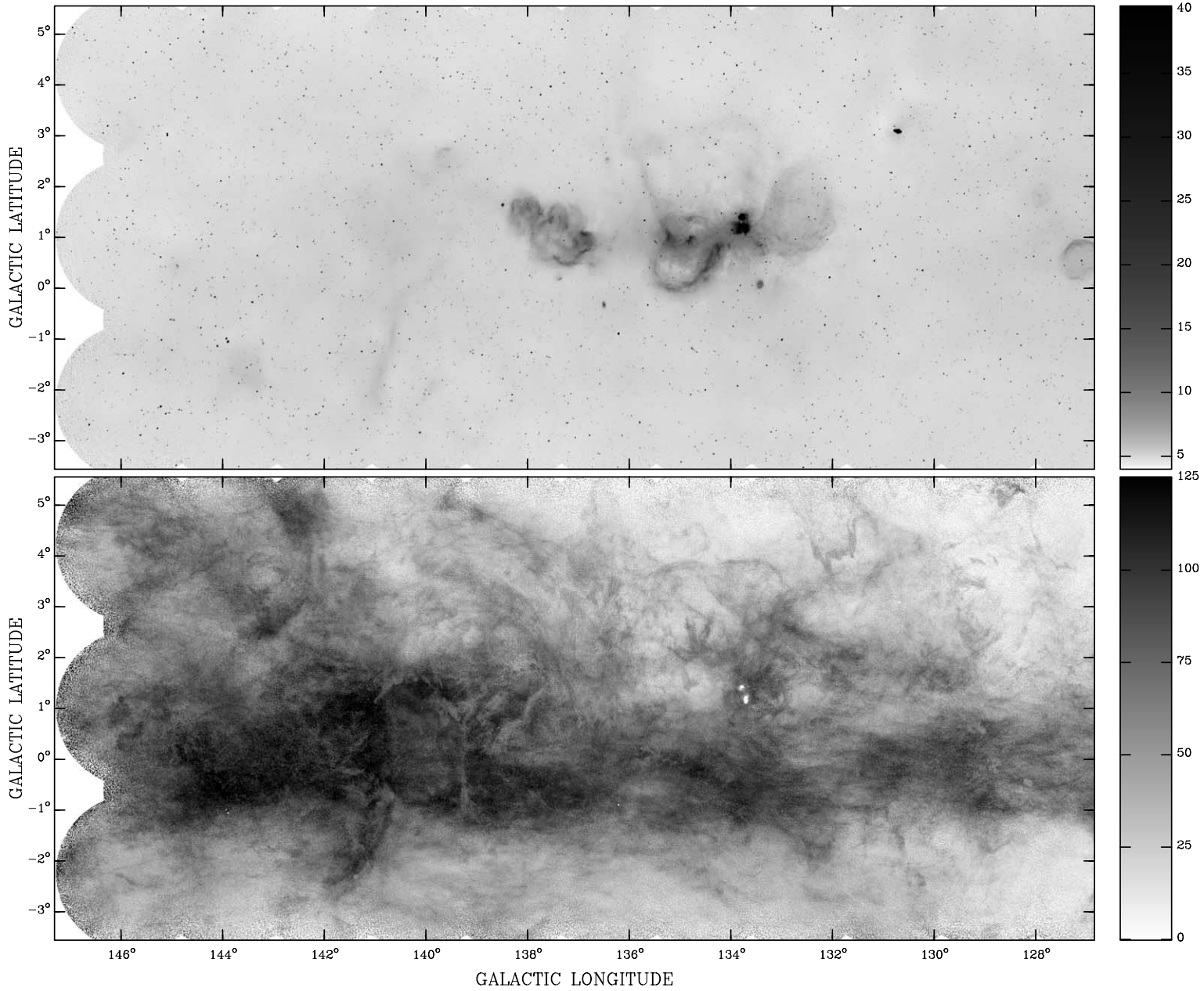

FIG. 7*a*

FIG. 7.—(*a*) Mosaic image covering the Galactic longitude range $127° \leq l \leq 147°$ from the DRAO 21 cm continuum data (*top*) and one channel of H I emission at $V_{LSR} = -40.21$ km s^{-1} (*bottom*). Both images are rendered as gray scale, with darker regions corresponding to higher intensity. The 21 cm continuum scale is logarithmic from $T_B = 4$ to $T_B = 40$ K. The H I emission scale is linear from $T_B = 0$ to $T_B = 125$ K. (*b–d*) Same as (*a*), except covering the Galactic longitude ranges $109° \leq l \leq 130°$, $92° \leq l \leq 112°$, and $74° \leq l \leq 94°$, respectively.

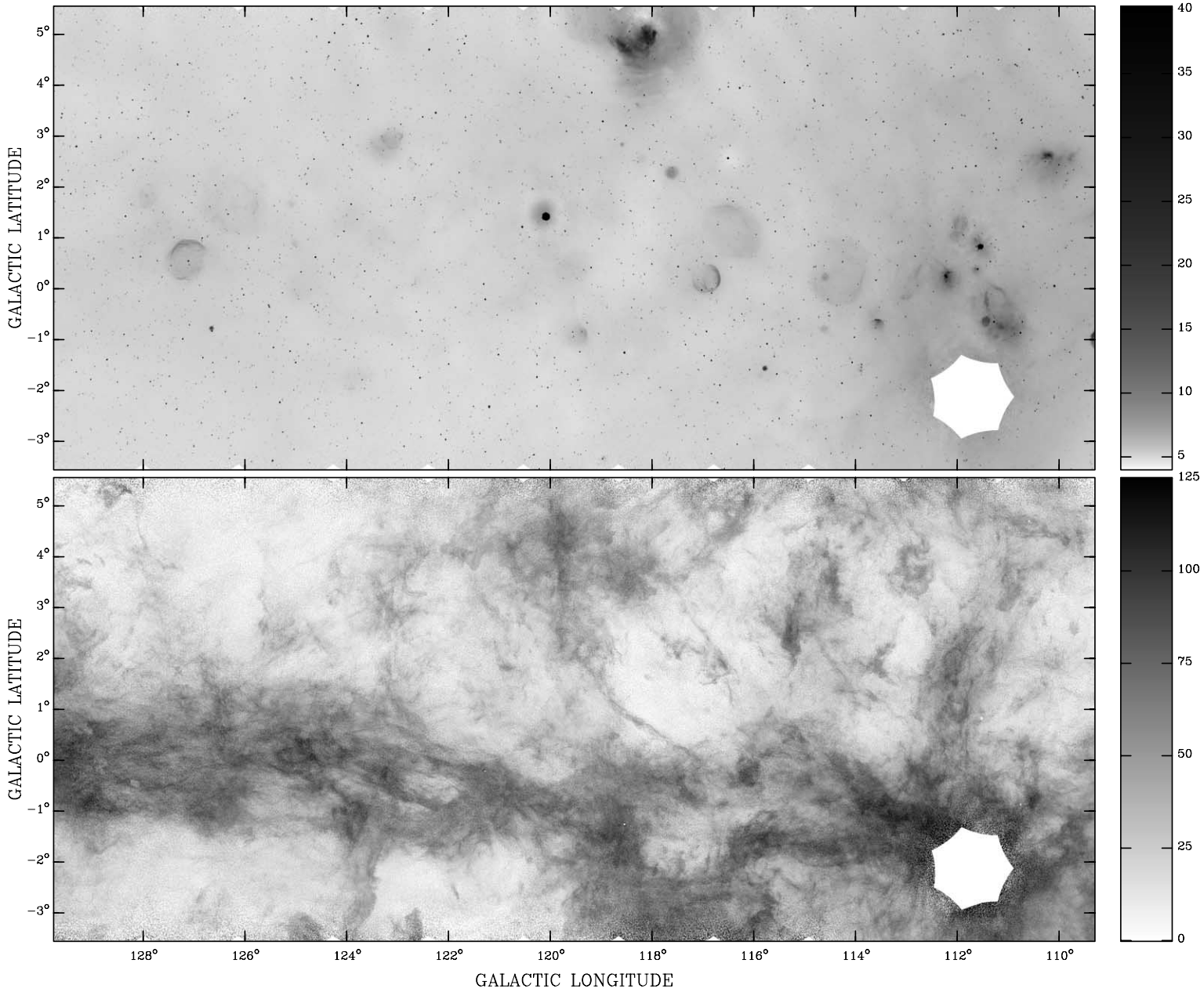
GALACTIC LATITUDE
5°
4°
3°
2°
1°
0°
−1°
−2°
−3°
40
35
30
25
20
15
10
5
GALACTIC LATITUDE
125
100
75
50
25
0
128°
126°
124°
122°
120°
118°
116°
114°
112°
110°
GALACTIC LONGITUDE

FIG. 7*b*

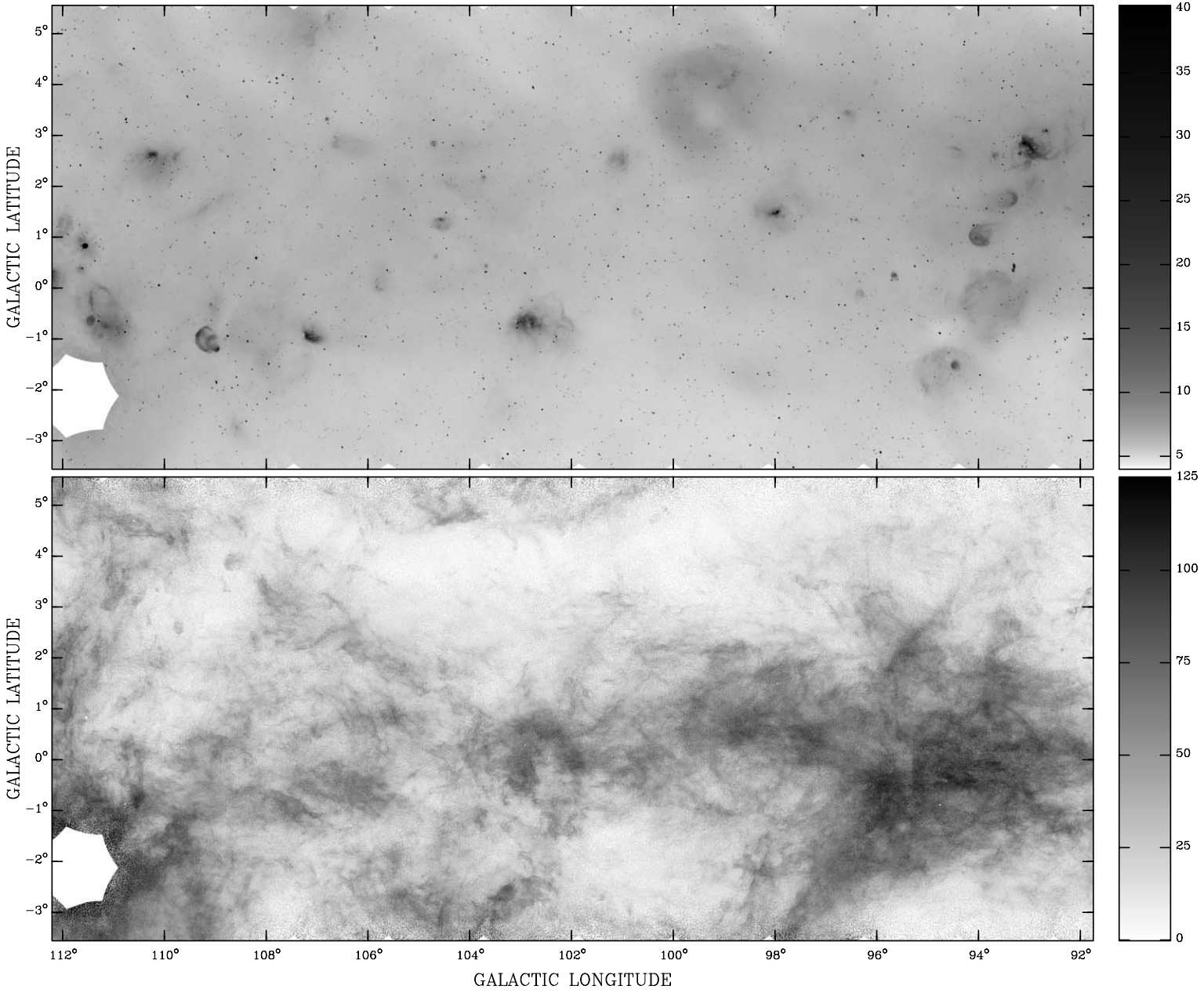
GALACTIC LATITUDE
5°
4°
3°
2°
1°
0°
−1°
−2°
−3°
40
35
30
25
20
15
10
5
GALACTIC LATITUDE
125
100
75
50
25
0
112°
110°
108°
106°
104°
102°
100°
98°
96°
94°
92°
GALACTIC LONGITUDE

FIG. 7*c*

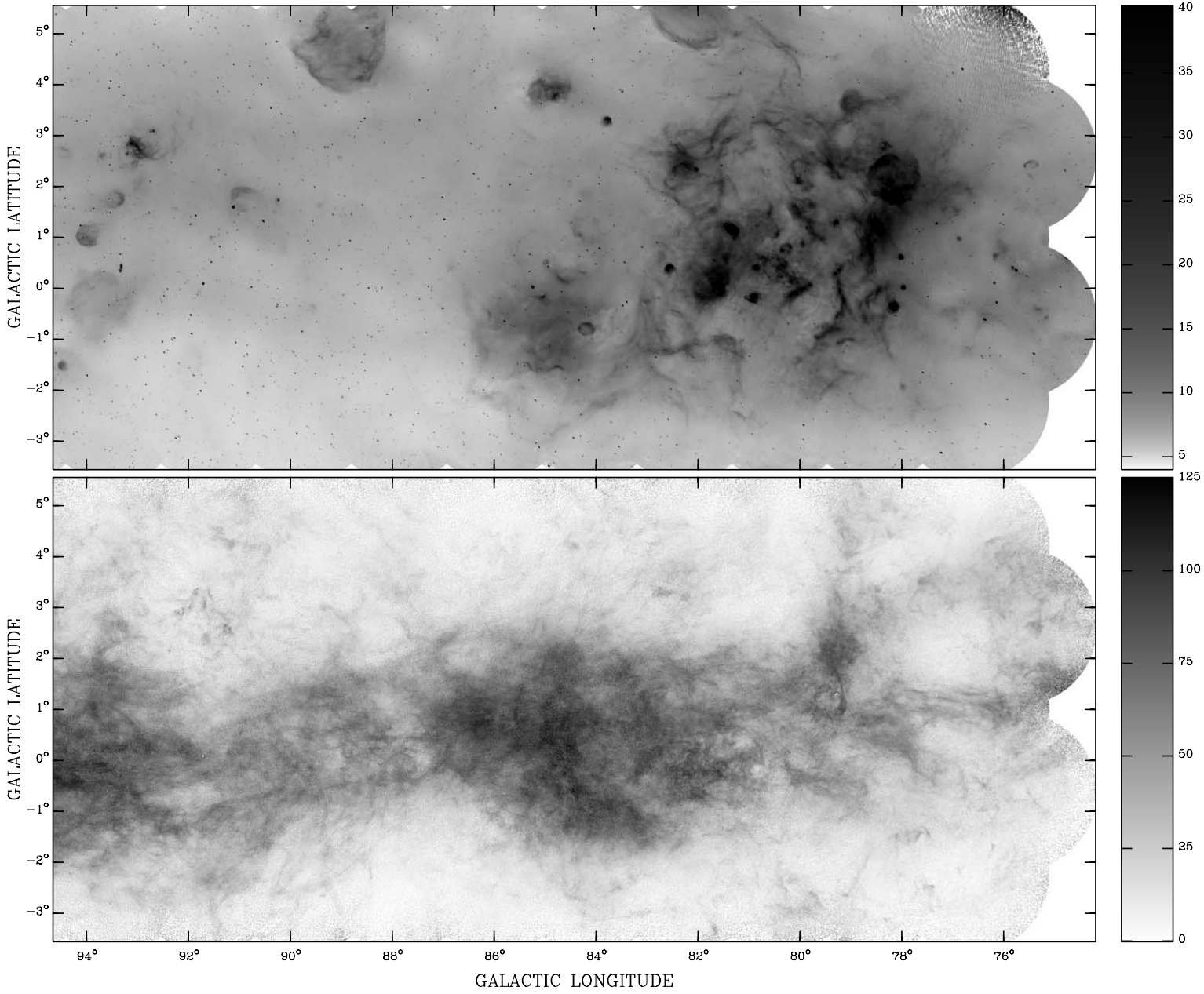
GALACTIC LATITUDE
5°
4°
3°
2°
1°
0°
−1°
−2°
−3°
40
35
30
25
20
15
10
5
125
100
75
50
25
0
94°
92°
90°
88°
86°
84°
82°
80°
78°
76°
GALACTIC LONGITUDE

FIG. 7*d*

The CGPS facilitates comparison of these low-frequency images to images of similar resolution at millimeter and infrared wavelengths, allowing systematic and wide-scale study of the relationship between the neutral atomic gas and the other states and phases of the ISM.

5. CGPS DATA PRODUCTS

5.1. *The CGPS Data Sets*

The final DRAO data products for the CGPS are the **M**-mosaics for all the frequency bands of the survey and **C**-mosaics at 408 MHz. The images are accompanied by auxiliary data including the weight images, beam-patch files, and resolution-parameter cubes.

The goal of the CGPS is to provide images of all the principal components of the ISM at similar angular resolution. The complete CGPS data set includes reprocessed data from surveys at millimeter and infrared wavelengths that are regridded to the CGPS **M**-series mosaic grid. Table 6 lists the survey data sets that make up the CGPS along with the ISM components traced by each.

The Five College Radio Astronomy Observatory (FCRAO) ^{12}CO (1–0) Outer Galaxy Survey (OGS; Heyer et al. 1998) provides our tracer for the molecular gas phase of the interstellar medium. The OGS coverage is $l = 102.^{\circ}5$ to $141.^{\circ}5$, $b = -3^{\circ}$ to $+5.^{\circ}4$, and $V_{\rm LSR} = -153$ to $+40$ km s^{-1}. For inclusion in the CGPS database the original OGS data have been reprocessed (Brunt & Ontkean 2003). The reprocessing suppresses correlated noise produced by sharing of reference measurements, estimates and removes contamination from emission in the reference positions, and fixes a number of other minor artifacts. The FCRAO data were convolved to $100.''44$ resolution (twice the OGS sampling) prior to reimaging onto the CGPS grid, on which 20 CGPS **M**-mosaics of ^{12}CO (1–0) emission have been constructed. The rms noise in the spectra is ~ 0.16 K (T_R^*), an improvement in sensitivity by a factor of about 4 from the original data.

Information on the dust component of the ISM is provided by two infrared atlases that are based on *IRAS* data: the *IRAS* Galaxy Atlas (IGA; 60 and 100 μm bands; Cao et al. 1997) and the Mid-Infrared Galaxy Atlas (MIGA; 12 and 25 μm bands; Kerton & Martin 2000). Over the CGPS survey region, Kerton & Martin have also extended the latitude coverage of the IGA to match that of the MIGA and meet the requirements for the **M**-mosaics. Both of these data sets consist of *IRAS* data processed using the HIRES algorithm (Aumann, Fowler, & Melnyck 1990) to achieve a typical resolution of $1'$. Special preprocessing steps and modifications to the original HIRES algorithm, described in Cao et al. (1996), allow the creation of high-quality, seamless, large-scale mosaics. The infrared data sets contained in the CGPS also include a number of ancillary files that provide the user with information about the achieved resolution, beam shape, *IRAS* scan pattern, and noise characteristics for a given mosaic.

5.2. *Sample CGPS Images*

Figure 8 shows the radio continuum products from the DRAO observations for the mosaic MW1 (see Table 3 and Fig. 4), including 1420 MHz Stokes *I*, 408 MHz Stokes *I*, 1420 MHz polarized intensity [calculated assuming $V = 0$, i.e., $(Q^2 + U^2)^{1/2}$], and polarization position angle. The bright filament of ionized gas running down the center of the 1420 MHz Stokes *I* image is Lynds Bright Nebula 679.

The polarized intensity image reveals highly structured polarized radiation distributed over almost the entire image. Outside of the region of LBN 679, bright polarized emission is seen with a wide range of spatial scales. This effect is ubiquitous in the CGPS images, and early results from polarization images have been reported by Gray et al. (1998, 1999). In general, structures seen in polarized emission are not replicated in total intensity, leading to the conclusion that the polarized emission is an effect of a foreground Faraday screen comprised of the magneto-ionic component of the ISM acting on emission from a smooth synchrotron background of Galactic origin. Such structures have also been seen with the Westerbork Synthesis Radio Telescope at 327 MHz (Wieringa et al. 1993) and the Australia Telescope at 1420 MHz (Gaensler et al. 2001). In Figure 8, the region coinciding with LBN 679 is seen to be depolarized. This effect can be attributed to beam depolarization in this high-n_e environment, where the Faraday rotation varies with angle on spatial scales smaller than the $1'$ beam (Peracaula et al. 1999).

TABLE 6
THE DATA SETS OF THE CGPS

ISM Component	Telescope	Wavelength	Angular Resolution	Coverage (l, b) (deg)	Coverage ($V_{\rm LSR}$) (km s^{-1})
Ionized and relativistic	DRAO[a]	73.4 cm	$3.'4 \times 3.'4$ cosec δ	$71.8 < l < 149.7, -6.7 < b < +8.7$	
Ionized and relativistic	DRAO[a]	21.1 cm	$49'' \times 49''$ cosec δ	$74.2 < l < 147.3, -3.6 < b < +5.6$	
Magneto-ionic medium.....	DRAO[a] (polarimetry)	21.1 cm	$58'' \times 58''$ cosec δ	$74.2 < l < 147.3, -3.6 < b < +5.6$	
Atomic (H I line)	DRAO[a]	21.1 cm	$58'' \times 58''$ cosec δ	$74.2 < l < 147.3, -3.6 < b < +5.6$	-150 to 50
Molecular (^{12}CO line).....	FCRAO[b]	2.6 mm	$100.''4$	$102.5 < l < 141.5, -3 < b < +5.4$	-153 to 40
Dust.....	*IRAS*[c]	100 μm	$1'$–$2'$	$0 < l < 360, -4.7 < b < +4.7$	
Dust.....	*IRAS*[c]	60 μm	$1'$–$2'$	$0 < l < 360, -4.7 < b < +4.7$	
Dust.....	*IRAS*[d]	25 μm	$\sim 0.'5$	$75 < l < 148, -6 < b < +6$	
Dust.....	*IRAS*[d]	12 μm	$\sim 0.'5$	$75 < l < 148, -6 < b < +6$	

[a] This paper.
[b] Heyer et. al. 1998.
[c] Reprocessed by California Institute of Technology (Cao et al. 1997).
[d] Reprocessed by the Canadian Institute for Theoretical Astrophysics (Kerton & Martin 2000).

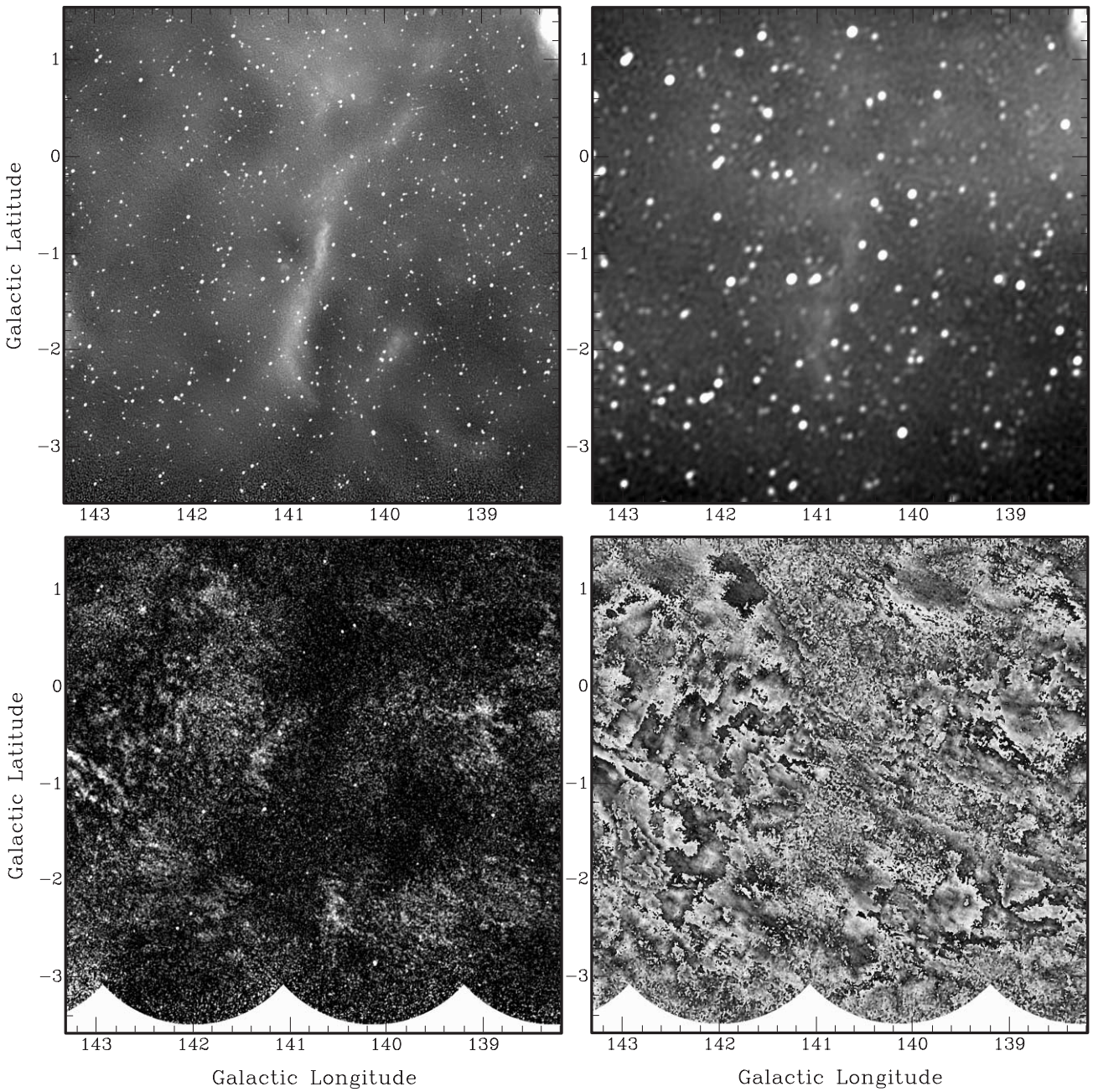

FIG. 8.—CGPS continuum images of the MW1 mosaic. The mosiac image is 5°.1 × 5°.1 centered at $(l, b) = (140°.75, -1°)$. The images show the four continuum products from the DRAO survey: 1420 MHz Stokes *I* continuum (*top left*), 408 MHz Stokes *I* continuum (*top right*), 1420 MHz polarized intensity (*bottom left*), and polarization position angle (*bottom right*).

The spatial structure in polarization angle that arises from the Faraday screen is readily visible in the polarization angle image. In this gray-scale representation of the polarization angle, the intensity goes from black to white along loci where the angle wraps from 180° to 0°. Regions bounded by these wrap contours represent areas where the polarization angle changes by less than 180° These "cells" thus define a spatial scale over which the rotation measure of the Faraday screen is relatively uniform.

Since the rotation measure of the Faraday screen is given by the product of electron density and magnetic field along the line of sight,

$$\mathrm{RM} = 8.1 \times 10^5 \int n_e B_{\parallel}\, dl \ \mathrm{rad\ m^{-2}}\ , \qquad (6)$$

knowledge of the average electron density from the bremsstrahlung emissivity allows information to be extracted on the interstellar magnetic field. The DRAO polarization observations at resolution $\sim 1'$ at 1420 MHz are well suited for studies of the random component of the magnetic field in the disk of the Galaxy. The excess rotation of the polarization angle by passage through a region of uniform electron density and magnetic field is given by $\Delta\psi = 46\lambda^2 n_e B_{\parallel} L$

degrees, where n_e has units of cm^{-3}, $B_\parallel$ μG, and L pc. The interstellar magnetic field is characterized by a uniform component and a random component with roughly equal magnitude of a few μG. Setting n_e and $B_\parallel$ to typical ISM values and $\lambda = 21$ cm yields

$$\Delta\psi = 42^\circ \left(\frac{n_e}{0.1\ \mathrm{cm}^{-3}}\right)\left(\frac{B_\parallel}{2\ \mu\mathrm{G}}\right)\left(\frac{L}{100\ \mathrm{pc}}\right). \qquad (7)$$

At typical distances of a few kpc, an angle of 1′ corresponds to a linear dimension of a few pc, and regions with dimension of tens to hundreds of pc will produce incremental rotation angles of a few tens to a few hundred degrees. Because of the λ^2 dependence, at shorter wavelengths the effect is much reduced and difficult to measure. At longer wavelengths rotation is so large that differential effects within the beam and along the line of sight lead to depolarization of signals at low latitudes, as noted by Wieringa et al. (1993).

Examination of the large 408 MHz, C1 mosaic in Figure 9 (see Table 5) underscores the very wide range of angular sizes present in the continuum structures seen in the Galactic plane. Very large diffuse structures of low surface brightness extend well beyond the boundaries of even this large image. The inset box in the image shows the region of the MW1 mosaic in Figure 9 containing the filamentary H II region from LBN 679. The H II complexes of W5 and W4 with surrounding diffuse halo are seen at the right side of the image. The background is dominated by a dense population of compact sources.

Figure 10 shows a set of CGPS images of the different components of the ISM from the DRAO (atomic hydrogen emission and ionized gas), FCRAO [^{12}CO (1–0)] and the IGA (dust emission at 60 μm). These varied images show complementary views of ISM features. For example, ionized gas and warm dust are plainly visible in the large, bright H II region W5 on the right side of the DRAO 1420 MHz continuum and IGA 60 μm panels. This feature is part of the W3/W4/W5 star-forming complex (e.g., Carpenter, Heyer, & Snell 2000) that extends farther to the east and contains numerous molecular clouds (Heyer & Terebey 1998), a few of which are visible in the ^{12}CO panel. In addition, the lower left corners of all four panels reveal different aspects of the Lynds Bright Nebula previously mentioned. This object, perhaps a giant shock structure, contains ionized gas, warm dust, molecular clouds, warm H I, and even indications of cold H I in self-absorption features.

The H I image in Figure 10 reveals a complex of dark filaments seen against the bright H I emission background.

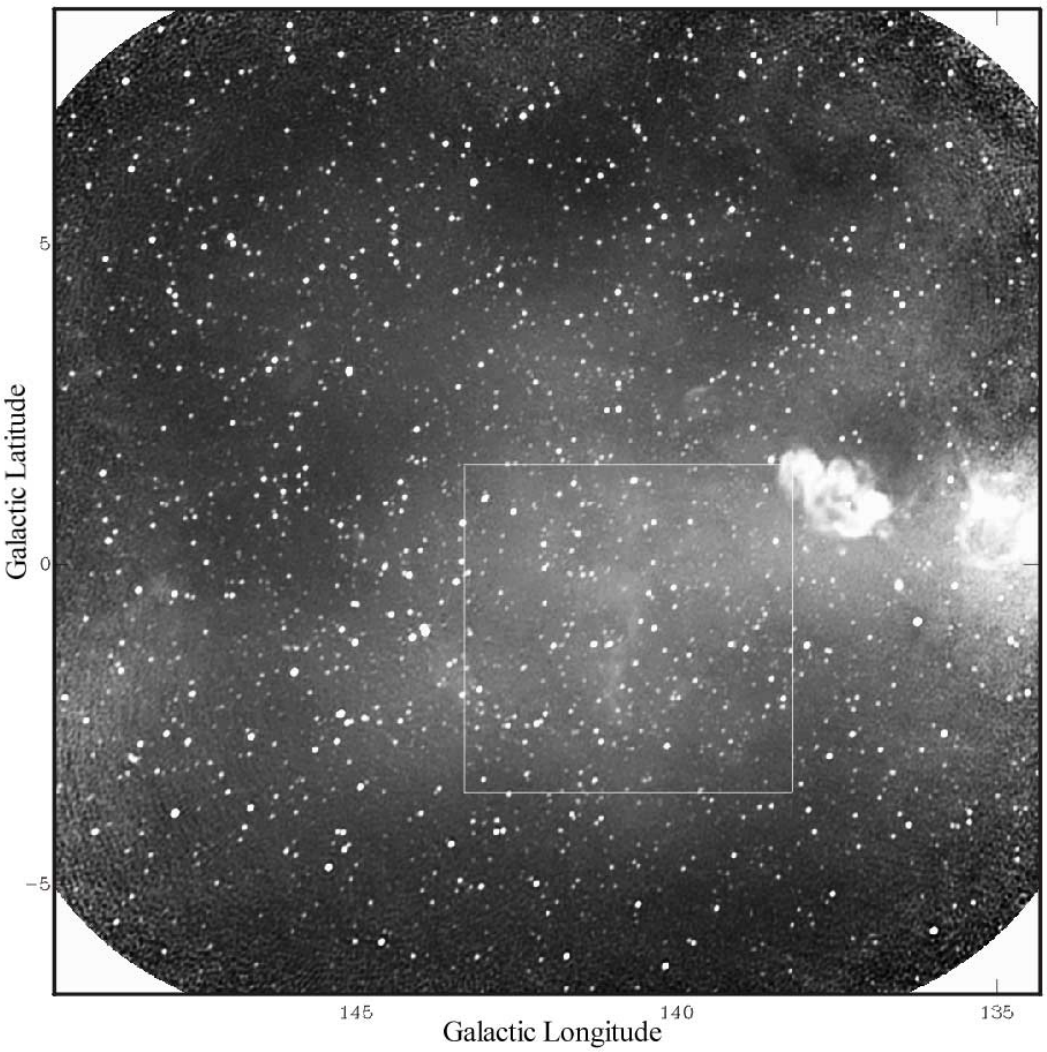

FIG. 9.—The 408 MHz Stokes I image for the 15° × 15° C1 mosaic (see Fig. 4). The white square delineates the area of mosaic MW1 (Fig. 8).

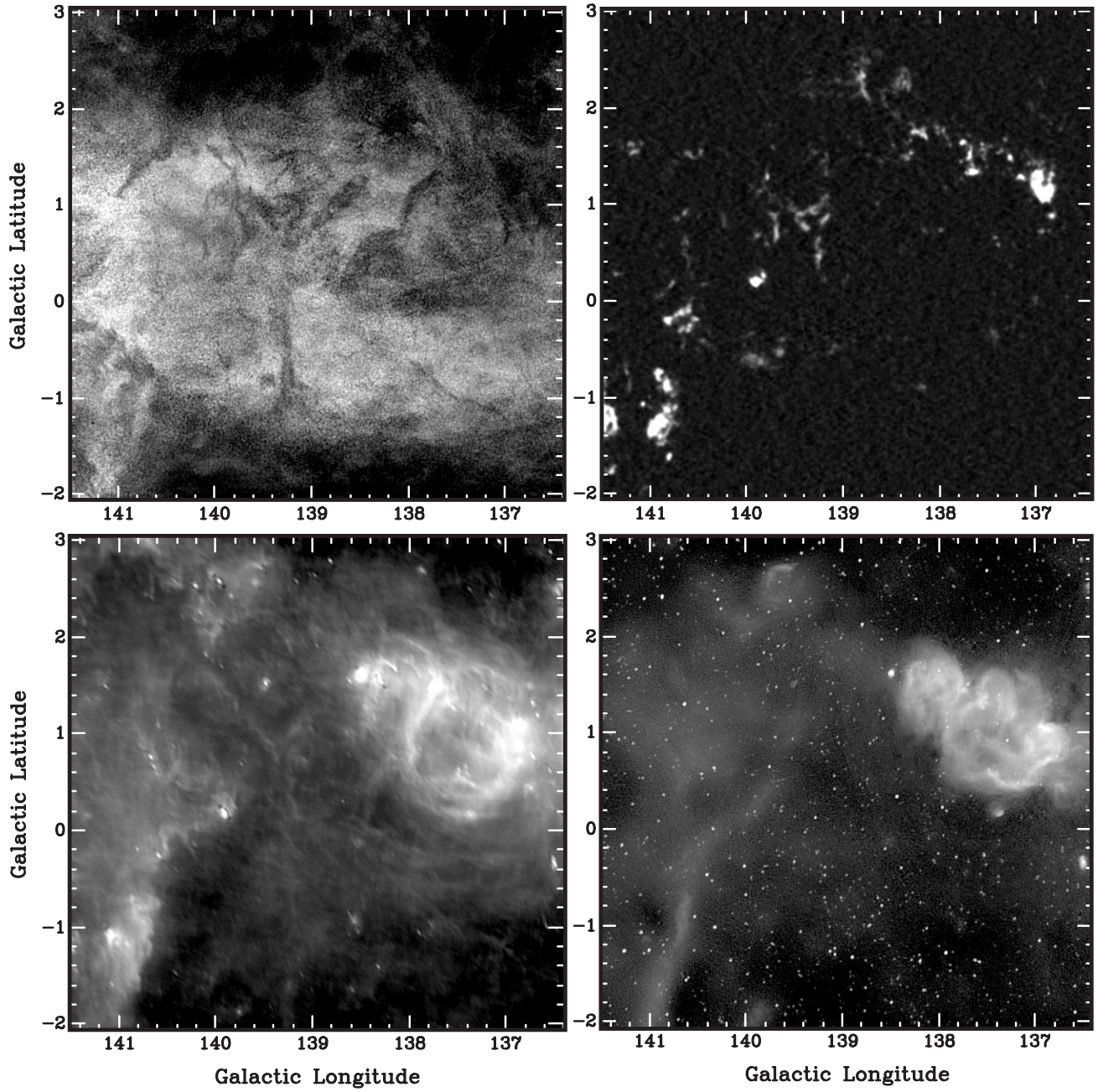

FIG. 10.—CGPS images of the same 5°.1 × 5°.1 region of the sky in atomic hydrogen emission from DRAO (*top left*), CO (1–0) from FCRAO (*top right*), dust emission at 60 μm emission from reprocessed *IRAS* data (*bottom left*), and ionized gas seen in $\lambda = 21$ cm continuum radiation from DRAO (*bottom right*). The H I and CO images show emission from gas moving with $V_{\rm LSR} = -41.04$ km s^{-1}. In all images lighter regions represent higher brightness emission. The dark filaments in the H I image are cold atomic hydrogen clouds absorbing the background H I emission. The bright radio continuum and dust emission region seen in the bottom panels is the W5 H II region. At the lower left in each image is the northern section of LBN 679, exhibiting emission from all of the ISM components.

These features are identified as self-absorption of the background emission by cold H I (HISA; Gibson et al. 2000). The spectral-line data features are too narrow in line width and too sharp in angular structure to be explained as physical gaps in a purely emissive H I medium (e.g. Baker & Burton 1979). A large-scale, high-resolution survey like the CGPS is required to systematically detect and map such structures. In the CGPS images a rich array of cold H I clouds is revealed throughout the Galactic plane as HISA, appearing wherever there is a sufficiently bright, smooth H I emission background against which such features may be distinguished (Gibson et al. 2000) and, in some instances, against a structured emission background (Knee & Brunt 2001).

Of particular interest in the context of the Galactic ISM is the relationship between the cold H I traced by HISA and the molecular gas and dust imaged at other wavelengths. A limited correspondence can be found in Figure 10 between some dark H I features and a few of the fainter molecular clouds and dust filaments, e.g., near $l = 139°.3$, $b = +0°.8$. While such associations can be identified throughout the survey, there is no general correlation between HISA and

CO line strengths (Gibson et al. 2003), as might be expected from traditional views of HISA tracing cold atomic gas in predominantly molecular clouds.

5.3. *Public Release of the CGPS Data*

The CGPS project has produced a unique data base designed to provide the means for systematic, multicomponent investigations of the phases and processes within the ISM over a broad range of spatial scales. The merged CGPS survey data sets have been publicly released in FITS format through the Canadian Astronomy Data Centre (CADC).[4]

For the DRAO data products, the individual Synthesis Telescope field data from the 193 synthesis observations are also available, as both image and visibility data sets. These data are also in FITS format, with the FITS-IDI (IDI = interferometry data interchange) format being used for the visibility data. These products include flux-registration corrections (either implicitly or explicitly), and position-registration corrections as comments, but do not include short-spacing complementary data.

[4] The CADC data archive can be accessed at http://cadc-ccda.hia-iha.nrc-cnrc.gc.ca/cgps.

The Dominion Radio Astrophysical Observatory is operated as a national facility by the National Research Council of Canada. The Canadian Galactic Plane Survey is a Canadian project with international partners. The Survey is supported by a grant from the Natural Sciences and Engineering Research Council of Canada. We also thank many present and former members of the DRAO staff for their skill and dedication in building, operating, and maintaining the Synthesis Telescope.

REFERENCES

Aumann, H. H., Fowler, J. W., & Melnyk, M. 1990, AJ, 99, 1674
Baars, J. W. M., Genzel, R., Pauliny-Toth, I. I. K., & Witzel, A. 1977, A&A, 61, 99
Baker, P. L., & Burton, W. B. 1979, A&AS, 35, 129
Bridle, A. H., & Schwab, F. R. 1989, in ASP Conf. Ser. 6, Synthesis Imaging in Radio Astronomy, ed. R. A. Perley, F. R. Schwab, & A. H. Bridle (San Francisco: ASP), 247
Brunt, C. M., & Ontkean, J. 2003, in preparation
Burton, W. B. 1985, A&AS, 62, 365
Cao, Y., Prince, T. A., Terebey, S., & Beichman, C. A. 1996, PASP, 108, 535
Cao, Y., Terebey, S., Prince, T. A., & Beichman, C. A. 1997, ApJS, 111, 387
Carpenter, J. M., Heyer, M. H., & Snell, R. L. 2000, ApJS, 130, 381
Condon, J. J., Cotton, W. D., Greisen, E. W., Yin, Q. F., Perley, R. A., Taylor, G. B., & Broderick, J. J. 1998, AJ, 115, 1693
Dennison, B., Topasna, G. A., & Simonetti, J. H. 1997, ApJ, 474, L31
Dickey, J. M., McClure-Griffiths, N., Gaensler, B., Green, A., Haynes, R., & Wieringa, M. 1999, in ASP Conf. Ser. 168, New Perspectives on the Interstellar Medium, ed. A. R. Taylor, T. L. Landecker, & G. Joncas (San Francisco: ASP), 27
Douglas, J. N., Bash, F. N., Bozyan, F. A., Torrence, G. W., & Wolfe, C. 1996, AJ, 111, 1945
English, J., Taylor, A. R., Mashchenko, S. Y., Irwin, J. A., Basu, S., & Johnstone, D. 2000, ApJ, 533, L25
Gaensler, B. M., Dickey, J. M., McClure-Griffiths, N. M., Green, A. J., Wieringa, M. H., & Haynes, R. F. 2001, ApJ, 549, 959
Gibson, S. J. 2002, in ASP Conf. Ser. 276, Seeing through the Dust: The Detection of H I and the Exploration of the ISM of Galaxies, ed. A. R. Taylor, T. L. Landecker, & A. G. Willis (San Francisco: ASP), 68
Gibson, S. J., Taylor, A. R., Higgs, L. A., Brunt, C. M., & Dewdney, P. E. 2003, in preparation
Gibson, S. J., Taylor, A. R., Higgs, L. A., & Dewdney, P. E. 2000, ApJ, 540, 851
Gray, A. D., Landecker, T. L., Dewdney, P. E., & Taylor, A. R. 1998, Nature, 393, 660
Gray, A. D., Landecker, T. L., Dewdney, P. E., Taylor, A. R., Willis, A. G., & Normandeau, M. 1999, ApJ, 514, 221
Hartmann, D., & Burton, W. B. 1997, Atlas of Galactic Neutral Hydrogen (Cambridge: Cambridge Univ. Press)
Haslam, C. G. T., Salter, C. J., Stoffel, H., & Wilson, W. E. 1982, A&AS, 47, 1
Heyer, M. H., Brunt, C. M., Snell, R. L., Howe, J. E., Schloerb, F. P., & Carpenter, J. M. 1998, ApJS, 115, 241
Heyer, M. H., & Terebey, S. 1998, ApJ, 502, 265
Higgs, L. A., & Tapping, K. F. 2000, AJ, 120, 2471
Johnston, K. J., et al. 1995, AJ, 110, 880
Kerton, C. R., & Martin, P. G. 2000, ApJS, 126, 85
Knee, L. B. G., & Brunt, C. M. 2001, Nature, 412, 308
Kothes, R., Landecker, T. L., Foster, T., & Leahy, D. A. 2001, A&A, 376, 641
Landecker, T. L., et al. 2000, A&AS, 145, 509
Normandeau, M., Taylor, A. R., & Dewdney, P. E. 1996, Nature, 380, 687
———. 1997, ApJS, 108, 279
Ott, M., Witzel, A., Quirrenbach, A., Krichbaum, T. P., Standje, K. J., Schalinski, C. J., & Hummel, C. A. 1994, A&A, 284, 331
Peracaula, M., Taylor, A. R., Bellchamber, T. L., Gray, A. D., & Landecker, T. L. 1999, in ASP Conf. Ser. 168, New Perspectives on the Interstellar Medium, ed. A. R. Taylor, T. L. Landecker, & G. Joncas (San Francisco: ASP), 86
Reich, P., & Reich, W. 1986, A&AS, 63, 205
Reich, P., Reich, W., & Fürst, E. 1997, A&AS, 126, 413
Reich, W. 1982, A&AS, 48, 219
Reich, W., Reich, P. & Fürst, E. 1990, A&AS, 83, 539
Roger, R. S., Bridle, A. H., & Costain, C. H. 1973, AJ, 78, 1030
Smegal, R. J., Landecker, T. L., Vaneldik, J. F., Routledge, D., & Dewdney, P. E. 1997, Radio Sci., 32, 643
Taylor, A. R., Stil, J. M., Dickey, J. M., McClure-Griffiths, N. M., Martin, P. G., Rothwell, T., & Lockman, J. 2002, in ASP Conf. Ser. 276, Seeing through the Dust: The Detection of H I and the Exploration of the ISM of Galaxies, ed. A. R. Taylor, T. L. Landecker, & A. G. Willis (San Francisco: ASP), 68
Vessey, S. J., & Green, D. A. 1998, MNRAS, 294, 607
Wieringa, M. H., de Bruyn, A. G., Jansen, D., Brouw, W. N., & Katgert, P. 1993, A&A, 268, 215
Willis, A. G. 1999, A&AS, 136, 603